

Cosmological prior for the J -factor estimation of dwarf spheroidal galaxies

Shun'ichi Horigome ^{1,a}, Kohei Hayashi ^{2,3,4,b}, and Shin'ichiro Ando ^{5,1,c}

¹ *Kavli IPMU (WPI), UTIAS, University of Tokyo, Kashiwa, Chiba, 277-8583, Japan*

² *National Institute of Technology, Ichinoseki College, Takanashi, Hagisho, Ichinoseki, Iwate, 021-8511, Japan*

³ *Astronomical Institute, Tohoku University, 6-3 Aoba, Aramaki, Aoba-ku, Sendai, Miyagi 980-8578, Japan*

⁴ *Institute for Cosmic Ray Research, The University of Tokyo, Chiba, 277-8582, Japan*

⁵ *GRAPPA Institute, Institute of Physics, University of Amsterdam, 1098 XH Amsterdam, The Netherlands*

Abstract

Dark matter halos of dwarf spheroidal galaxies (dSphs) play important roles in dark matter detection. Generally we estimate the halo profile using a kinematical equation of dSphs but the halo profile has a large uncertainty because we have only a limited number of kinematical dataset. In this paper, we utilize cosmological models of dark matter subhalos to obtain better constraints on halo profile of dSphs. The constraints are realized as two cosmological priors: satellite prior, based on a semi-analytic model of the accretion history of subhalos and their tidal stripping effect, and stellar-to-halo mass relation prior, which estimates halo mass of a galaxy from its stellar mass using empirical correlations. In addition, we adopt a radial dependent likelihood function by considering velocity dispersion profile, which allows us to mitigate the parameter degeneracy in the previous analysis using a radial independent likelihood function with averaged dispersion. Using these priors, we estimate the squared dark matter density integrated over the region-of-interest (so-called J -factor) of 8 classical and 27 ultra-faint dSphs. Our method significantly decreases the uncertainty of J -factors (upto about 20%) compared to the previous radial independent analysis. We confirm the model dependence of J -factor estimates by evaluating Bayes factors of different model setups and find that the estimates are still stable even when assuming different cosmological models.

^ashunichi.horigome@ipmu.jp

^bkohei.hayashi@g.ichinoseki.ac.jp

^cs.ando@uva.nl

Contents

1	Introduction	1
2	Method	2
2.1	Models and likelihood	2
2.2	Priors	4
2.2.1	Photometry prior	4
2.2.2	Satellite prior	4
2.2.3	SHMR prior	5
2.3	Data	7
2.4	Analysis	9
3	Results	9
4	Discussion	14
4.1	Posterior	14
4.2	J -factor and Bayes factor	15
5	Summary and conclusion	16
A	Posteriors	17

1 Introduction

The presence of dark matter in our universe is one of the most important open questions in the current physics. Even though cosmological observations agree with predictions of Λ -cold dark matter (CDM) model with surprising accuracy [1], we still do not know what dark matter is. In order to answer this question, many candidates and detection methods have been proposed [2]. Among various detection methods, those using dwarf spheroidal galaxies (dSphs) are interesting. DSpes are a kind of satellite galaxy of the Milky Way with large mass-to-light ratio, which implies that they are dark matter rich objects. Such a large amount of dark matter enables us to explore the nature of dark matter. In the indirect detection method, we can constrain the annihilation cross section by observing signal flux of annihilation products. This method is very useful to detect well-motivated dark matter candidates such as the weakly interacting massive particles (WIMPs) [3, 4], because they have large annihilation cross section thanks to a non-relativistic quantum effect, so-called the Sommerfeld effect [5, 6]. The sensitivity of the detection depends on the estimated amount of signal flux. This amount is proportional to an astrophysical quantity, so-called J -factor:

$$J(\Delta\Omega) \equiv \int d\Omega \int dl \rho^2(r) \quad (1)$$

where Ω is the solid angle, $\Delta\Omega$ is the region-of-interest, l denotes the line-of-sight distance, r is the radius from the center of a target dSph, and $\rho(r)$ denotes the dark matter density profile. In order to obtain reliable and useful results, we need to know the accurate and precise value of J -factor, that is, the shape of dark matter density profile $\rho(r)$.

Although dSphs are useful tools to study the dark matter, their dark matter density profiles have large astrophysical uncertainty compared to other uncertainties from particle physics models. Generally, the dark matter density profile is estimated by fitting spectroscopic data set of dSph member stars using the Jeans equation [7]. However, the stellar data set cannot completely determine the dark matter profile because we generally use empirical models of the dark matter profile through the fitting and their parameters are degenerated. Fortunately, from the viewpoint of cosmology, structure formation models predict the distribution of dSph profiles in the universe, which is useful to select theoretically favored density profile model parameters and mitigate the problematic degeneracy. For instance, Ref. [8] use the conventional theory of spherical collapse to roughly constrain the parameter space of dark matter density profile.

Recently, semi-analytic models of the tidal mass striping effect on the cold dark matter halo are developed [9, 10], which allows us to construct a multivariate distribution of dSph mass and its tidal truncation radius. This probability distribution was applied as a prior (called *satellite prior*) for the J -factor estimation of dSphs by fitting their averaged velocity dispersion [11] and it was shown that the satellite prior has a potential to break the degeneracy among parameters of the NFW profile [12].

While the satellite prior gives a statistical trend for the whole dSphs, cosmology offers us another way to constrain the dark matter mass of individual dSph. Since the dark matter plays an essential role to form the structure of the universe including dSphs, the stellar components of dSphs has a strong relation to their dark matter halo, known as the stellar-to-halo mass relation (SHMR) [13]. The dark matter halo mass in each dSph can be therefore constrained by its stellar mass by using this relation.

In this paper, we perform a more detailed analysis of the satellite prior in Ref. [11]

(hereafter SA20) by considering the radial dependence of the velocity dispersion to optimize given kinematical data sets. The radial dependency weakens the degeneracy among dark matter halo parameters and gives more precise estimation than the radial independent analysis. Moreover, we consider some SHMR models to obtain more reasonable estimation results from the viewpoint of cosmology. These models help us to obtain more accurate constraints of the halo parameters than the previous satellite prior only analysis. From the other point of view, our analysis also provides a method for evaluating the credibility of each SHMR model using dark matter halos of dSphs. This paper is organized as follows: In Section 2, we discuss our analysis method. In Section 2.1, we describe our model setups and assumptions on the dSph system and introduce our likelihood function. In Section 2.2, we explain the construction of the satellite prior and the stellar-to-halo mass relation prior. We set up several choice of these prior reflecting the uncertainty of cosmological models. In Section 2.3, we show the table of dSphs including their half-light radii and distances. The kinematical data set and preanalysis method for each dSph is also described. In Section 3, we show results of the analysis and estimated J -factor values. Here we compare results of different priors to verify the stability of estimated J -factor by changing cosmological models. In Section 5, we discuss and summarize our results.

2 Method

2.1 Models and likelihood

We assume that dSphs are spherical and steady systems according to conventional analyses¹ [8, 15]. Their velocity dispersions are determined by the spherical Jeans equation

$$\frac{1}{\nu(r)} \frac{\partial(\nu(r)\sigma_r^2(r))}{\partial r} + 2\sigma_r^2(r)\beta(r) = -\frac{GM(r)}{r^2}, \quad (2)$$

where G is the gravitational constant, r denotes the distance from the dSph center, $\nu(r)$ is the stellar number density and $M(r)$ denotes the dark matter mass enclosed within the radius r . The anisotropy of the stellar motion $\beta(r)$ is defined by the ratio of the velocity dispersions $\sigma_r^2(r)$, $\sigma_\theta^2(r)$ and $\sigma_\phi^2(r)$ as $\beta(r) \equiv 1 - \frac{\sigma_\theta^2 + \sigma_\phi^2}{2\sigma_r^2}$. By definition, $\beta(r)$ satisfies $-\infty < \beta(r) \leq 1$. In this paper, we assume that $\beta(r) = \beta_{\text{ani}}$ (const.) for simplicity.

We describe the stellar profile $\nu(r)$ as the Plummer profile, a widely-used fitting function of the stellar number density of dSphs [16].² Its stellar number density $\nu(r)$ and surface density $\Sigma(R)$ are given by

$$\nu(r) = \frac{3}{4\pi R_e^3} \left(1 + \left(\frac{r}{R_e} \right)^2 \right)^{-5/2}, \quad (3)$$

$$\Sigma(R) = \frac{1}{\pi R_e^2} \left(1 + \frac{R^2}{R_e^2} \right)^{-2}, \quad (4)$$

¹The sphericity of dSphs is also assumed when deriving the satellite prior [11]. However, Ref. [14] suggests that axisymmetric models show better fitting performance than spherical models in terms of Bayes factor comparison. Hence, further study on the axisymmetric formalization of the satellite prior would be useful for future J -factor analyses, which is however beyond the scope of this paper.

²Note that the stellar profile fitting by using generalized function suggests that some dSphs have multiple components. [17, 18]

where R denotes the radius projected on the celestial sphere and R_e is the half-light radius of the surface density profile.

For the dark matter density profile, there are many discussions and no consensus exists yet. This is known as the core-cusp problem [19]; N-body simulation shows the cuspy dark matter density profile ($\rho(r) \propto r^{-1}$ around the center), while observations suggest the cored profile ($\rho(r) \propto \text{const.}$). In this paper, we assume the cold dark matter model, then the dark matter density profile can be well described by the truncated NFW profile [12], whose mass density $\rho(r)$ and enclosed mass $M(r) \equiv \int dr 4\pi r^2 \rho(r)$ are respectively written as

$$\rho(r) = \begin{cases} \rho_s \left(\frac{r}{r_s}\right)^{-1} \left(1 + \frac{r}{r_s}\right)^{-2} & (0 \leq r \leq r_t) \\ 0 & (r_t < r) \end{cases}, \quad (5)$$

$$M(r) = \begin{cases} 4\pi \rho_s r_s^3 f_{\text{NFW}}(r/r_s) & (0 \leq r \leq r_t) \\ 4\pi \rho_s r_s^3 f_{\text{NFW}}(r_t/r_s) & (r_t < r), \end{cases} \quad (6)$$

where ρ_s and r_s is scale density and radius of the profile, respectively, r_t denotes the truncation radius, and an auxiliary function $f_{\text{NFW}}(x)$ is defined as follows:

$$f_{\text{NFW}}(x) = \ln(1+x) - \frac{1}{1+x^{-1}}. \quad (7)$$

Using these quantities, we define our likelihood function as follows:

$$\mathcal{L}(\Theta) = \prod_i \mathcal{N}[v_i; v_{\text{dSph}}, \sigma_{\text{los}}^2(R_i) + \delta\sigma_i^2], \quad (8)$$

where v_{dSph} is the systemic velocity of each dSph, $\Theta \equiv \{R_e, r_s, \rho_s, r_t, \beta_{\text{ani}}, v_{\text{dSph}}\}$ represents the parameter set in our model, $\mathcal{N}[x; \mu, \sigma^2]$ denotes the normal (Gaussian) distribution with the mean μ and the variance σ^2 , v_i is the observed velocity of i -th star and $\delta\sigma_i$ is its observational error. The function $\sigma_{\text{los}}^2(R)$ is the projected velocity dispersion along the line-of-sight at projected radius R , given by the following formula:

$$\sigma_{\text{los}}^2(R) = \frac{2}{\Sigma(R)} \int_R^\infty dr \left(1 - \beta(r) \frac{R^2}{r^2}\right) \frac{\nu(r) \sigma_r^2(r)}{\sqrt{1 - R^2/r^2}}. \quad (9)$$

When $\beta(r) = \beta_{\text{ani}}$ (const.), Eq. (9) is simplified to [20]

$$\sigma_{\text{los}}^2(R) = \frac{1}{\Sigma(R)} \int_R^\infty ds \nu(s) \frac{GM(s)}{s} K(s/R), \quad (10)$$

$$K(u) = \sqrt{1-u^{-2}} \left[u^2 \left(\frac{3}{2} - \beta_{\text{ani}} \right) {}_2F_1 \left(1, \frac{3}{2} - \beta_{\text{ani}}; \frac{3}{2}; 1-u^2 \right) - \frac{1}{2} \right]. \quad (11)$$

where ${}_2F_1(a, b; c; z)$ is the Gaussian hypergeometric function.

We note that our likelihood function has R -dependence in contrast with that SA20 used the averaged (R -independent) velocity dispersion $\overline{\sigma_{\text{los}}^2} = \frac{4\pi G}{3} \int_0^\infty dr r \nu(r) M(r)$. The advantage of the our R -dependent analysis is that it weakens the degeneracy between parameters by probing the shape of $\sigma_{\text{los}}^2(R)$ even when $\overline{\sigma_{\text{los}}^2}$ is not changed.

2.2 Priors

2.2.1 Photometry prior

The half-light radius R_e is constrained by the result of photometric observations, which is realized as a photometric prior. We adopt log-normal distribution for the half-light radius to construct the prior as follows:

$$\pi_{\text{photo.}}(\log_{10} R_e / [\text{pc}]) = \mathcal{N}(\log_{10} R_e / [\text{pc}] | \log_{10} r_{e,\text{circ}} / [\text{pc}], \delta \log_{10} r_{e,\text{circ}} / [\text{pc}]), \quad (12)$$

where we calculate the mean $\log_{10} r_{e,\text{circ}}$ and standard deviation $\delta \log_{10} r_{e,\text{circ}}$ based on the error propagation law by using $\hat{\theta}$ listed in Table. 1 on the supplement material of SA20.³

2.2.2 Satellite prior

Structure formation models of subhalos in Milky Way predict structural parameters of subhalo profile $\rho(r)$: r_s , ρ_s and r_t . In this paper we use the satellite prior proposed in SA20, briefly reviewed in the following: The formation of subhalos are well described by the extended Press-Schechter formalism [21], which gives the differential number of accreted subhalos $\frac{d^2 N_{\text{sh}}}{dz_a dm_a}$. Here N_{sh} denotes the number of subhalo, z_a and m_a are the redshift and mass of a subhalo when the subhalo accreted onto its host. Here m_a can be reinterpreted as halo parameters $\rho_{s,a}$, $r_{s,a}$ and r_{200} by considering two conditions: i.) The subhalo is virialized $m_a = 4\pi\rho_{\text{crit}}(z_a)200r_{200}^3/3$, where the virial radius r_{200} is calculated from $r_{s,a}$ by using the concentration parameter $c_a = r_{s,a}/r_{200}$, whose probability density distribution $P(c_a)$ is given by the log-normal distribution with mean $c_{200}(m_a, z_a)$ [22] and standard deviation $\sigma_{\ln c} = 0.13$ [23]. ii.) The dark matter distribution of the subhalo is given by the NFW profile $m_{200} = 4\pi\rho_{s,a}r_s^3f_{\text{NFW}}(r_{200}/r_{s,a})$, where f_{NFW} is the same as defined in Eq. (7).

After the accretion, the tidal force of Milky Way starts striping subhalo mass. In a semi-analytic strategy, the mass-loss rate through this process is modeled as

$$\frac{dm}{dt} = -A \frac{m(z)}{\tau_{\text{dyn}}(z)} \left[\frac{m(z)}{M(z)} \right]^{\zeta} \quad (13)$$

where $\tau_{\text{dyn}}(z)$ denote the dynamical timescale [24], $m(z)$ and $M(z)$ are subhalo and host halo mass at redshift z , respectively. The two parameters A and ζ are calibrated by the results of N-body simulations. The solution of this equation with the initial condition $m(z_a) = m_a$ gives current ($z = 0$) subhalo mass $m_0 = m(0)$. As the subhalo mass evolve, structural parameters $\rho_{s,a}$ and $r_{s,a}$ also evolve to $\rho_{s,0}$ and $r_{s,0}$ (or simply ρ_s and r_s) according empirical fitting formula [23]. Finally, current truncation radius $r_{t,0}$ (or simply r_t) are determined by the NFW condition $m_0 = 4\pi\rho_{s,0}r_{s,0}^3f_{\text{NFW}}(r_{t,0}/r_{s,0})$.

We combine the two distributions of parameters at accretion $\frac{d^2 N_{\text{sh}}}{dz_a dm_a}$ and $P(c_a)$ with the parameter evolution model to obtain the distribution of parameters at present.⁴ Instead of calculating the distribution of current parameters directly by using the Jacobian of the

³In SA20 they assume the normal distribution for the half-light radius, but we found no significant difference between the normal and log-normal distributions because the standard deviation is so small that the log-normal distribution can be approximated by the normal distribution. In this paper, we adopt log-normal distribution, reflecting the fact that the radius must be positive.

⁴Here we assume that there are no correlation between (m_a, z_a) and $c_{t,a}$.

evolution formula, we obtain finite samples of the parameters. We subdivide $(\ln m_a, z_a, c_a)$ linearly and calculate the weight of i -th grid according to

$$w_i = N \frac{d^2N_{sh}}{dz_a dm_a} \Bigg|_{z_a=z_{a,i}, m_a=m_{a,i}} (\Delta z_a)_i (\Delta m_a)_i P(c_a) \Bigg|_{c_a=c_{a,i}} (\Delta c_a)_i \quad (14)$$

where N is a normalization factor to satisfy the condition $\sum_i w_i = N_{sh,\text{tot}} \equiv \int \int dz_a dm_a \frac{d^2N_{sh}}{dz_a dm_a}$. Each point $(\ln m_{a,i}, z_{a,i}, c_{a,i})$ is interpreted to $(\rho_{s,i}, r_{s,i}, c_{t,i})$ according to the stripping model, then we obtain finite samples of (ρ_s, r_s, c_t) with its weight.⁵

Some subhalos do not host any stars because baryons in too small a halo cannot lose their energy due to its ionizing background, known as reionization suppression [25, 26]. In order to consider the effect, we multiply w_i by the formation probability of a satellite for the given subhalo P_{form} , as follows:

$$P_{\text{form}}(V_{\text{peak}}) = \frac{1}{2} \left[1 + \text{erf}\left(\frac{V_{\text{peak}} - V_{50}}{\sqrt{2}\sigma}\right) \right], \quad (15)$$

where V_{peak} denotes the maximum circular velocity of the satellite at accretion time, given by $V_{\text{peak}} = (4\pi G \rho_{s,a} / 4.625)^{1/2} r_{s,a}$ for a NFW subhalo and it is calculated for each parameter grid $(\rho_{s,i}, r_{s,i}, c_{t,i})$. For the lower bound parameter V_{50} , we have two choices: $V_{50} = 18 \text{ km/s}$, motivated by conventional theory of reionization [27–30], and $V_{50} = 10.5 \text{ km/s}$, based on the result of more recent analysis [26]. For σ , we adopt $\sigma = 2.5 \text{ km s}^{-1}$, following Ref. [26]. For classical dSphs, we adopt $V_{50} = 25 \text{ km/s}$ according to [31]. Here we assume $\sigma = 0 \text{ km s}^{-1}$ for simplicity. In this case $P_{\text{form}}(V_{\text{peak}})$ is equivalent to a step function $\Theta(V_{\text{peak}} - V_{50})$.

Using these quantities, the probability density distribution of the three profile parameters is then given by

$$\pi_{\text{sat.}}(r_s, \rho_s, r_t) \propto \frac{d^3N_{sh}}{dr_s dr_s dr_t} P_{\text{form}}(V_{\text{peak}}), \quad (16)$$

where $\pi_{\text{sat.}}$ should be properly normalized to be a probability density distribution function. For the discrete sample points generated above, it is realized as

$$\pi_{\text{sat.,i}} = \frac{w_i P_{\text{form}}(V_{\text{peak},i})}{\sum_i w_i P_{\text{form}}(V_{\text{peak},i})}. \quad (17)$$

Finally we smooth these samples $\{\pi_{\text{sat.,i}}\}$ to reconstruct a prior function $\pi_{\text{sat.}}(r_s, \rho_s, r_t)$ by using weighted kernel density estimation implemented in `scipy` [32].

2.2.3 SHMR prior

In addition to the satellite prior, we use another prior motivated by the stellar-to-halo mass relation (SHMR) (see [33] for a review). This relation is obtained by fitting the structure formation model by using observed cosmological data sets with a simple assumption; the larger halo becomes, the more stars it hosts. Stellar mass m_* is then written as a monotonic function of halo mass m_z for given redshift z . We identify $m(z)$ with the subhalo mass at the accretion time and relate it to the current subhalo mass using the semi-analytic approach

⁵Available in https://github.com/shinichiroando/dwarf_params. More integrated version named SASHIMI is in <https://github.com/shinichiroando/sashimi-c>.

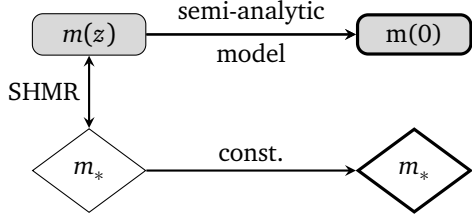


Figure 1: A schematic picture to illustrate how to construct our SHMR prior. Horizontal one-side arrows indicate time evolution. Shapes with bold edges are values at present ($z = 0$), appeared in the definition of the SHMR prior in Eq. (18).

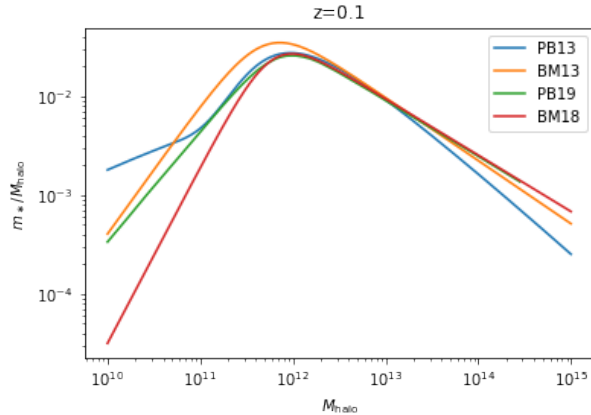


Figure 2: SHMR function $m_*(M_h, z)$ normalized by the halo mass M_h . Here we fix $z = 0.1$ for illustration purpose.

mentioned in Section 2.2.2. Here, for the simplicity, we assume that the stellar mass does not change after accretion and identify m_* as the current stellar mass.⁶ The schematic figure of this procedure is shown in Fig. 1.

In order to check model dependence, we adopt four SHMR models [34–37] (hereafter **PB13**, **BM13**, **PB19** and **BM18**, respectively). These model have the following features:

- **PB13**: calibrated by the Bolshoi simulation, using a multi-power law fitting function for the SHMR and fitting the SHMR intrinsic parameters with other systematic parameters.
- **BM13**: calibrated by the Millennium simulation, using a double-power law fitting function for the SHMR and simply fitting SHMR parameters.
- **PB19**: updated data sets from **PB13**, cosmological models calibrated by the Bolshoi-Planck simulation, using a double-power law fitting function for the SHMR and simply fitting SHMR parameters.
- **BM18**: updated data sets from **BM13**, cosmological models assuming double-power law for the evolution of baryon conversion efficiency calibrated by an independent

⁶Basically, a galaxy is hosted at the center of a dark matter halo which is more massive than stellar mass, and the tidal force strips mainly the dominant component of the halo mass. Therefore stellar mass is not significantly changed until the most of halo mass is striped and halo mass and galaxy mass become comparable. However, once the halo mass becomes comparable, it cannot bound the galaxy within the halo and the galaxy gets collapsed, thus we cannot find such galaxies anymore.

simulation, using double-power law for the SHMR and simply fitting SHMR parameters.

The probability density distribution of stellar mass m_* is then written as follows:

$$P(m_*|m(z)) = \mathcal{N}[m_*; m_*(m(z), z), \delta m_*] \quad (18)$$

where $m_*(M_h, z)$ is expected stellar mass for given halo mass M_h at accretion redshift z . δm_* denotes the model uncertainty of each SHMR model. We show the function $m_*(M_h, z)$ for each model in Fig. 2.

In terms of the Bayesian statistics, we can compare credibility of a model (model 1) to a reference model (model 0) by using Bayes factor BF, defined as the ratio of Bayesian evidences \mathcal{E} :

$$BF = \frac{\mathcal{E}_1}{\mathcal{E}_0} = \frac{\int d\Theta_1 \mathcal{L}_1(\Theta_1) \pi_1(\Theta_1)}{\int d\Theta_0 \mathcal{L}_0(\Theta_0) \pi_0(\Theta_0)}. \quad (19)$$

Here the minus logarithm of the Bayesian evidence $-\ln \mathcal{E}$ is approximated by the widely applicable Bayesian information criterion (WBIC) [38]:

$$-\ln \mathcal{E} \simeq WBIC = -\frac{\int d\Theta (\ln \mathcal{L}(\Theta)) \mathcal{L}(\Theta)^\beta \pi(\Theta)}{\int d\Theta \mathcal{L}(\Theta)^\beta \pi(\Theta)}, \quad (20)$$

$$\beta = 1 / \ln(\#data). \quad (21)$$

In this work, we calculate WBIC of each model using the MCMC algorithm and evaluate the Bayes factor according to

$$\ln BF = \ln \mathcal{E}_1 - \ln \mathcal{E}_0 \simeq -WBIC_1 + WBIC_0. \quad (22)$$

Here $BF > 1$ or $\ln BF > 0$ means that model 1 is more credible than model 0. According to Ref. [39], there is a scale for interpreting $\ln BF$ into the strength of evidence as follows: *Decisive* for $\ln BF \gtrsim 4$, *very strong* for $3 \lesssim \ln BF \lesssim 4$, *strong* for $2 \lesssim \ln BF \lesssim 3$, *substantial* for $1 \lesssim \ln BF \lesssim 2$, and *barely worth mentioning* for $0 \lesssim \ln BF \lesssim 1$.

2.3 Data

We analyze the dSphs listed in Tables 1 and 2 according to SA20, where we show the half-light radius, distance, and stellar mass of each dSph. The half-light radius and distances are from SA20 and also we use the values in Ref. [40] for the stellar masses. For dSphs without stellar mass values in Ref. [40], we calculate their stellar masses from apparent magnitudes and distances, assuming $M/L = 1$ according to Ref. [40]. The last column in Tables 1 and 2 indicates references of the kinematical data set. In general, kinematical data set includes member stars and foreground stars. For data sets having membership flag, we extract stars identified as members. For those containing membership probability P_M , we choose member-like stars ($P_M > 0.95$). For the other data sets having no membership information, we adopt the selection criteria illustrated and described in the reference. In addition, we remove member stars identified as binary stars in order to avoid accidental increase of the velocity dispersion.

Table 1: The half-light radius, distance from Earth, stellar mass and reference list for the 27 ultra-faint dSphs analyzed in this paper. We derive the half-light radius and its error based on the value in SA20. The values of distance and stellar mass are from SA20 and Ref. [40], respectively (see text for more details). The last column shows the source of kinematical data set.

Name	$\log_{10} R_e/[\text{pc}]$	$D_*[\text{kpc}]$	$M_* [M_\odot]$	Refs.
Aquarius 2	2.09 ± 0.08	108	4.7×10^3	[41]
Boötes 1	2.20 ± 0.02	66	2.9×10^4	[42]
Boötes 2	1.52 ± 0.07	42	1.0×10^3	[43, 44]
CanesVenatici 1	2.53 ± 0.02	218	2.3×10^5	[45]
CanesVenatici 2	1.73 ± 0.09	160	7.9×10^3	[45]
Carina 2	1.87 ± 0.05	36	5.4×10^3	[46]
ComaBerenices	1.76 ± 0.03	44	3.7×10^3	[45]
Draco 2	1.12 ± 0.18	20	1.0×10^3	[47]
Eridanus 2	2.20 ± 0.05	380	6.5×10^4	[48]
Grus 1	1.27 ± 0.46	120	2.1×10^3	[49]
Hercules	2.08 ± 0.04	132	3.7×10^4	[45]
Horologium 1	1.49 ± 0.10	79	2.2×10^3	[50]
Hydrus 1	1.73 ± 0.03	28	6.5×10^3	[51]
Leo 4	2.01 ± 0.05	154	1.9×10^4	[45, 52]
Leo T	2.13 ± 0.05	417	1.4×10^5	[45]
Leo 5	1.57 ± 0.18	178	1.1×10^4	[52]
Pegasus 3	1.62 ± 0.16	215	3.6×10^3	[53]
Pisces 2	1.68 ± 0.07	182	8.6×10^3	[54]
Reticulum 2	1.49 ± 0.02	30	3.0×10^3	[55]
Segue 1	1.30 ± 0.06	23	3.4×10^2	[56]
Segue 2	1.53 ± 0.04	35	8.6×10^2	[57]
Triangulum 2	1.10 ± 0.13	30	4.5×10^2	[58]
Tucana 2	2.21 ± 0.07	57	2.8×10^3	[49]
Tucana 3	1.64 ± 0.06	25	7.9×10^2	[59]
UrsaMajor 1	2.18 ± 0.02	97	1.4×10^4	[45]
UrsaMajor 2	1.93 ± 0.02	32	4.1×10^3	[45]
Willman 1	1.30 ± 0.05	38	1.0×10^3	[60]

Table 2: Same as Table 1, but for classical dSphs.

Name	$\log_{10} R_e/[\text{pc}]$	$D_*[\text{kpc}]$	$M_* [M_\odot]$	Refs.
Carina	2.392 ± 0.005	105	3.8×10^5	[61]
Draco	2.256 ± 0.005	76	2.9×10^5	[62]
Fornax	2.849 ± 0.003	147	2.0×10^7	[61]
Leo 1	2.353 ± 0.004	254	5.5×10^6	[63]
Leo 2	2.217 ± 0.005	233	7.4×10^5	[64]
Sculptor	2.359 ± 0.004	86	2.3×10^6	[61]
Sextans 1	2.538 ± 0.004	86	4.4×10^5	[61]
UrsaMinor	2.434 ± 0.006	76	2.9×10^5	[65]

Table 3: Scanning region of each parameter.

parameter	min.	max.
$\log_{10} R_e/\text{[pc]}$	1.0	3.5
$\log_{10} r_s/\text{[pc]}$	0.0	5.0
$\log_{10} \rho_s/\text{[M}_\odot\text{pc}^{-3}]$	-4.0	4.0
$\log_{10} r_t/\text{[pc]}$	0.0	5.0
$-\log_{10}(1 - \beta_{\text{ani}})$	-1.0	1.0
$v_{\text{dSph}}/\text{[km s}^{-1}\text{]}$	-1000	1000

2.4 Analysis

Based on the likelihood and priors defined above, we can calculate the posterior probability density distribution (or simply posterior) $P(\Theta|D)$ by using the Bayes' theorem:

$$P(\Theta|D) = \frac{\mathcal{L}(\Theta)\pi(\Theta)}{\int d\Theta \mathcal{L}(\Theta)\pi(\Theta)}, \quad (23)$$

where

$$\pi = \begin{cases} \pi_{\text{photo.}} & (\text{without any cosmological priors}) \\ \pi_{\text{photo.}}\pi_{\text{sat.}} & (\text{satellite prior only}) \\ \pi_{\text{photo.}}\pi_{\text{sat.+SHMR}} & (\text{satellite \& SHMR prior}) \end{cases} \quad (24)$$

Here, as mentioned in Section 2.2, the satellite prior $\pi_{\text{sat.}}$ is selected from two candidates sat._{10.5} and sat.₁₈, and the SHMR model for $\pi_{\text{sat.+SHMR}}$ is chosen from PB13, BM13, PB19 and BM18.

Instead of calculating Eq. (23) straightforwardly, we obtain samples from the posterior by using the Markov Chain Monte-Carlo methods. In this paper, we use the Affine invariant ensemble sampler implemented in emcee [66]. We scan the parameter region as shown in Table 3. For R_e , r_s , ρ_s and r_t we adopt the logarithmic scale, reflecting that they are positive. The range for the anisotropy β_{ani} is set to include both of radial and tangential cases. Since v_{dSph} is strongly constrained by the likelihood function, we choose its limits large enough to include the estimated value.

3 Results

Figure 3 shows the posterior projected onto r_s - ρ_s plane. The value of likelihood function is shown by blue dots and contours. Colored contours denote posteriors assuming the satellite and/or SHMR priors. The satellite prior itself is shown by gray contours and gray shaded area shows the cosmological constraint adopted in Ref. [8]. For illustration purpose, we only show the result of Segue 1. For other dSphs, see Figs. 7 and 8.

In order to clarify the advantage of R -dependent analysis, we compare results of R -dependent and R -independent likelihood analyses in Fig. 4, where R -independent likelihood is defined similarly to Eq. (8) but the velocity dispersion $\sigma_{\text{los}}^2(R)$ is replaced by averaged dispersion $\overline{\sigma_{\text{los}}^2}$. In Fig. 4 the color of the heat map corresponds to the value of likelihood functions.

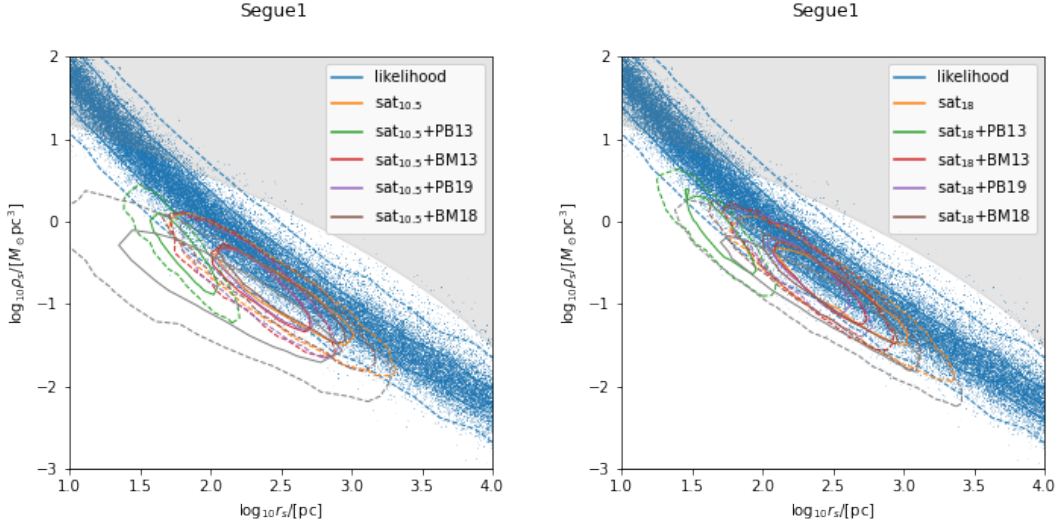


Figure 3: Posterior probability density function projected onto r_s - ρ_s plain for the case of Segue 1. The left and right panels show result assuming the sat._{10.5} and sat.₁₈ model, respectively. Blue dots are distributed according to likelihood only analysis (without any cosmological priors), while colored contours show posteriors with cosmological priors. Gray shaded area shows the cosmological constraint adopted in Ref. [8]. For the other dSphs, see Figs. 7 and 8.

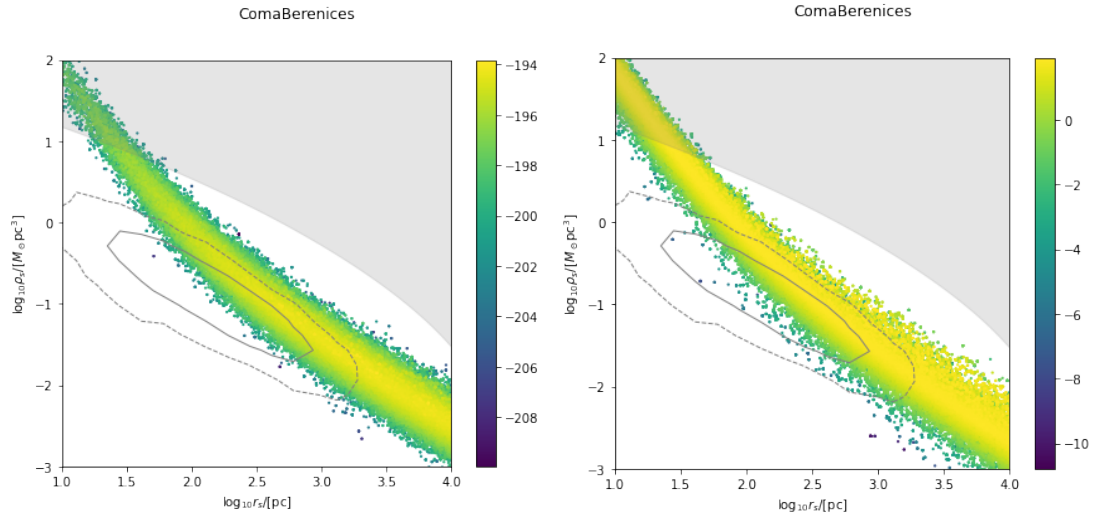


Figure 4: Results of likelihood only (without any cosmological priors) analyses. The left panel is for the R -dependent likelihood function, (Eq. (8)), while the right panel is for the R -independent likelihood (see text), respectively. Color of heat map corresponds to the value of profiled likelihood function $\mathcal{L}_{\text{prof}}(r_s, \rho_s) \equiv \max_{r_t} \mathcal{L}(r_s, \rho_s, r_t)$. Gray contours denote the 1σ and 2σ regions of the satellite prior and gray shaded region shows the rough cosmological prior adopted in Ref. [8]. For illustration purpose, we show only the Coma Berenices case.

Table 4: Median and 1σ interval of the estimated J -factors. sat._{10.5} and sat.₁₈ denote the satellite prior assuming $V_{50} = 10.5$ and 18 km/s , respectively.

	w/o SHMR	flat	sat. _{10.5}	sat. ₁₈	sat. _{10.5}	sat. ₁₈	sat. _{10.5}	sat. ₁₈	sat. _{10.5}	sat. ₁₈							
PB13																	
Aquarius2	$18.25^{+0.61}_{-0.55}$	$17.62^{+0.37}_{-0.36}$	$17.84^{+0.35}_{-0.36}$	$17.21^{+0.26}_{-0.24}$	$17.31^{+0.26}_{-0.24}$	$17.57^{+0.31}_{-0.32}$	$17.73^{+0.34}_{-0.37}$	$17.71^{+0.31}_{-0.35}$	$17.80^{+0.31}_{-0.35}$	$17.92^{+0.34}_{-0.33}$	$17.91^{+0.33}_{-0.34}$						
Bootes1	$18.24^{+0.28}_{-0.26}$	$18.03^{+0.22}_{-0.21}$	$18.11^{+0.18}_{-0.21}$	$17.95^{+0.19}_{-0.18}$	$17.99^{+0.17}_{-0.17}$	$18.09^{+0.21}_{-0.21}$	$18.09^{+0.21}_{-0.21}$	$18.12^{+0.22}_{-0.20}$	$18.12^{+0.22}_{-0.21}$	$18.31^{+0.19}_{-0.18}$	$18.30^{+0.17}_{-0.17}$						
Bootes2	$16.64^{+2.80}_{-4.90}$	$17.69^{+0.65}_{-0.81}$	$18.41^{+0.46}_{-0.53}$	$17.48^{+0.28}_{-0.29}$	$17.53^{+0.32}_{-0.29}$	$17.64^{+0.53}_{-0.49}$	$17.84^{+0.69}_{-0.67}$	$17.74^{+0.58}_{-0.73}$	$18.33^{+0.39}_{-0.42}$	$18.33^{+0.41}_{-0.38}$	$18.35^{+0.44}_{-0.41}$						
CanesVenatici1	$17.59^{+0.32}_{-0.19}$	$17.42^{+0.13}_{-0.12}$	$17.45^{+0.12}_{-0.12}$	$17.41^{+0.13}_{-0.12}$	$17.45^{+0.14}_{-0.12}$	$17.45^{+0.11}_{-0.12}$	$17.44^{+0.12}_{-0.12}$	$17.47^{+0.12}_{-0.12}$	$17.46^{+0.13}_{-0.12}$	$17.46^{+0.10}_{-0.07}$	$17.46^{+0.10}_{-0.07}$						
CanesVenatici2	$17.94^{+0.50}_{-0.45}$	$17.40^{+0.37}_{-0.36}$	$17.58^{+0.30}_{-0.31}$	$16.98^{+0.23}_{-0.25}$	$17.08^{+0.23}_{-0.25}$	$17.38^{+0.27}_{-0.31}$	$17.48^{+0.27}_{-0.32}$	$17.47^{+0.27}_{-0.28}$	$17.51^{+0.27}_{-0.28}$	$17.68^{+0.30}_{-0.31}$	$17.68^{+0.30}_{-0.30}$						
Carina2	$18.38^{+0.56}_{-0.54}$	$18.06^{+0.41}_{-0.37}$	$18.35^{+0.37}_{-0.36}$	$18.00^{+0.25}_{-0.26}$	$18.06^{+0.26}_{-0.25}$	$18.15^{+0.33}_{-0.32}$	$18.18^{+0.39}_{-0.36}$	$18.17^{+0.39}_{-0.42}$	$18.39^{+0.33}_{-0.35}$	$18.53^{+0.30}_{-0.27}$	$18.56^{+0.30}_{-0.27}$						
ComaBerenices	$18.95^{+0.36}_{-0.36}$	$18.58^{+0.28}_{-0.29}$	$18.70^{+0.26}_{-0.26}$	$18.13^{+0.23}_{-0.23}$	$18.19^{+0.24}_{-0.23}$	$18.49^{+0.25}_{-0.27}$	$18.60^{+0.24}_{-0.26}$	$18.55^{+0.25}_{-0.27}$	$18.63^{+0.23}_{-0.24}$	$18.71^{+0.26}_{-0.26}$	$18.71^{+0.26}_{-0.27}$						
Draco2	$16.80^{+2.54}_{-4.77}$	$18.30^{+0.62}_{-0.78}$	$18.93^{+0.43}_{-0.49}$	$18.12^{+0.29}_{-0.29}$	$18.15^{+0.29}_{-0.27}$	$18.28^{+0.49}_{-0.48}$	$18.40^{+0.69}_{-0.61}$	$18.35^{+0.54}_{-0.70}$	$18.89^{+0.37}_{-0.43}$	$18.90^{+0.37}_{-0.35}$	$18.93^{+0.38}_{-0.35}$						
Eridanus2	$17.29^{+0.38}_{-0.36}$	$16.91^{+0.25}_{-0.24}$	$16.98^{+0.24}_{-0.23}$	$16.76^{+0.20}_{-0.19}$	$16.81^{+0.19}_{-0.19}$	$16.97^{+0.22}_{-0.22}$	$16.96^{+0.22}_{-0.22}$	$17.03^{+0.21}_{-0.21}$	$17.03^{+0.23}_{-0.23}$	$17.15^{+0.14}_{-0.14}$	$17.14^{+0.14}_{-0.15}$						
Grus1	$17.42^{+0.88}_{-0.89}$	$17.09^{+0.46}_{-0.48}$	$17.44^{+0.44}_{-0.44}$	$16.77^{+0.26}_{-0.25}$	$16.85^{+0.28}_{-0.26}$	$17.05^{+0.42}_{-0.41}$	$17.26^{+0.46}_{-0.50}$	$17.15^{+0.41}_{-0.48}$	$17.43^{+0.36}_{-0.39}$	$17.53^{+0.37}_{-0.36}$	$17.51^{+0.39}_{-0.35}$						
Hercules	$17.89^{+0.37}_{-0.37}$	$17.51^{+0.30}_{-0.27}$	$17.69^{+0.28}_{-0.27}$	$17.43^{+0.21}_{-0.21}$	$17.48^{+0.22}_{-0.23}$	$17.62^{+0.26}_{-0.27}$	$17.61^{+0.26}_{-0.25}$	$17.69^{+0.26}_{-0.29}$	$17.69^{+0.27}_{-0.28}$	$17.93^{+0.18}_{-0.20}$	$17.95^{+0.18}_{-0.21}$						
Horologium1	$19.08^{+0.68}_{-0.63}$	$18.11^{+0.41}_{-0.40}$	$18.26^{+0.37}_{-0.37}$	$17.53^{+0.24}_{-0.23}$	$17.59^{+0.25}_{-0.23}$	$17.95^{+0.31}_{-0.31}$	$18.18^{+0.30}_{-0.30}$	$18.05^{+0.31}_{-0.34}$	$18.18^{+0.28}_{-0.30}$	$18.25^{+0.35}_{-0.36}$	$18.29^{+0.34}_{-0.36}$						
Hydrus1	$18.52^{+0.36}_{-0.32}$	$18.33^{+0.29}_{-0.27}$	$18.50^{+0.31}_{-0.28}$	$18.25^{+0.21}_{-0.19}$	$18.30^{+0.21}_{-0.21}$	$18.37^{+0.26}_{-0.26}$	$18.38^{+0.31}_{-0.26}$	$18.42^{+0.29}_{-0.26}$	$18.51^{+0.25}_{-0.26}$	$18.68^{+0.25}_{-0.22}$	$18.68^{+0.25}_{-0.22}$						
Leo4	$15.63^{+1.85}_{-5.06}$	$16.72^{+0.53}_{-0.61}$	$17.17^{+0.47}_{-0.46}$	$16.96^{+0.27}_{-0.27}$	$17.01^{+0.27}_{-0.27}$	$17.09^{+0.39}_{-0.39}$	$17.15^{+0.37}_{-0.37}$	$16.95^{+0.53}_{-0.50}$	$17.18^{+0.43}_{-0.47}$	$17.70^{+0.28}_{-0.27}$	$17.69^{+0.27}_{-0.27}$						
Leo5	$17.18^{+0.78}_{-0.82}$	$16.92^{+0.45}_{-0.48}$	$17.28^{+0.36}_{-0.43}$	$16.73^{+0.27}_{-0.26}$	$16.87^{+0.26}_{-0.26}$	$17.07^{+0.34}_{-0.34}$	$17.16^{+0.37}_{-0.37}$	$17.17^{+0.36}_{-0.36}$	$17.29^{+0.32}_{-0.32}$	$17.51^{+0.30}_{-0.30}$	$17.51^{+0.33}_{-0.31}$						
LeoT	$17.61^{+0.43}_{-0.44}$	$16.95^{+0.31}_{-0.31}$	$17.01^{+0.27}_{-0.29}$	$16.82^{+0.22}_{-0.22}$	$16.87^{+0.23}_{-0.23}$	$17.07^{+0.26}_{-0.26}$	$17.09^{+0.24}_{-0.24}$	$17.12^{+0.26}_{-0.30}$	$17.12^{+0.27}_{-0.32}$	$17.06^{+0.10}_{-0.12}$	$17.05^{+0.10}_{-0.10}$						
Pegasus3	$17.82^{+1.01}_{-2.10}$	$16.72^{+0.60}_{-0.61}$	$17.23^{+0.44}_{-0.46}$	$16.41^{+0.29}_{-0.27}$	$16.45^{+0.31}_{-0.31}$	$16.78^{+0.46}_{-0.46}$	$17.00^{+0.50}_{-0.49}$	$16.88^{+0.47}_{-0.50}$	$17.17^{+0.35}_{-0.47}$	$17.35^{+0.39}_{-0.47}$	$17.35^{+0.39}_{-0.39}$						
Pisces2	$17.24^{+0.91}_{-1.17}$	$16.74^{+0.55}_{-0.56}$	$17.15^{+0.46}_{-0.48}$	$16.70^{+0.27}_{-0.27}$	$16.72^{+0.30}_{-0.30}$	$16.87^{+0.42}_{-0.38}$	$16.94^{+0.47}_{-0.45}$	$16.93^{+0.48}_{-0.60}$	$17.15^{+0.42}_{-0.42}$	$17.47^{+0.33}_{-0.36}$	$17.50^{+0.34}_{-0.34}$						
Reticulum2	$18.98^{+0.37}_{-0.36}$	$18.65^{+0.30}_{-0.30}$	$18.80^{+0.27}_{-0.28}$	$18.31^{+0.21}_{-0.20}$	$18.35^{+0.21}_{-0.20}$	$18.57^{+0.27}_{-0.28}$	$18.70^{+0.29}_{-0.28}$	$18.68^{+0.25}_{-0.28}$	$18.75^{+0.25}_{-0.26}$	$18.81^{+0.27}_{-0.27}$	$18.82^{+0.26}_{-0.27}$						
Segue1	$19.74^{+0.39}_{-0.41}$	$19.20^{+0.33}_{-0.39}$	$19.32^{+0.32}_{-0.33}$	$18.36^{+0.31}_{-0.33}$	$18.95^{+0.30}_{-0.31}$	$19.23^{+0.27}_{-0.30}$	$18.98^{+0.30}_{-0.34}$	$18.98^{+0.34}_{-0.34}$	$19.21^{+0.25}_{-0.25}$	$19.23^{+0.30}_{-0.30}$	$19.23^{+0.30}_{-0.31}$						
Segue2	$18.02^{+0.70}_{-2.06}$	$18.01^{+0.46}_{-0.50}$	$18.42^{+0.37}_{-0.41}$	$17.66^{+0.26}_{-0.26}$	$17.72^{+0.27}_{-0.28}$	$17.93^{+0.40}_{-0.44}$	$18.11^{+0.44}_{-0.60}$	$18.11^{+0.37}_{-0.51}$	$18.37^{+0.30}_{-0.37}$	$18.38^{+0.32}_{-0.30}$	$18.39^{+0.35}_{-0.34}$						
Triangulum2	$14.36^{+2.91}_{-3.86}$	$17.75^{+0.67}_{-0.66}$	$18.54^{+0.43}_{-0.49}$	$17.56^{+0.29}_{-0.28}$	$17.63^{+0.27}_{-0.28}$	$17.68^{+0.55}_{-0.55}$	$17.96^{+0.65}_{-0.65}$	$17.77^{+0.57}_{-0.70}$	$18.44^{+0.36}_{-0.42}$	$18.43^{+0.37}_{-0.38}$	$18.39^{+0.43}_{-0.36}$						
Tucana2	$18.14^{+0.58}_{-0.52}$	$17.87^{+0.38}_{-0.36}$	$18.16^{+0.36}_{-0.35}$	$17.57^{+0.26}_{-0.25}$	$17.68^{+0.25}_{-0.23}$	$17.84^{+0.33}_{-0.30}$	$18.02^{+0.36}_{-0.35}$	$17.96^{+0.33}_{-0.35}$	$18.10^{+0.32}_{-0.32}$	$18.20^{+0.32}_{-0.30}$	$18.19^{+0.32}_{-0.29}$						
Tucana3	$15.71^{+1.79}_{-4.35}$	$17.52^{+0.45}_{-0.56}$	$18.06^{+0.34}_{-0.33}$	$17.73^{+0.25}_{-0.27}$	$17.80^{+0.26}_{-0.25}$	$17.63^{+0.35}_{-0.29}$	$17.65^{+0.35}_{-0.30}$	$17.53^{+0.46}_{-0.38}$	$18.05^{+0.43}_{-0.50}$	$18.29^{+0.27}_{-0.27}$	$18.25^{+0.27}_{-0.23}$						
UrsaMajor1	$18.66^{+0.30}_{-0.29}$	$18.30^{+0.22}_{-0.22}$	$18.34^{+0.20}_{-0.20}$	$18.03^{+0.21}_{-0.19}$	$18.09^{+0.19}_{-0.20}$	$18.26^{+0.20}_{-0.20}$	$18.27^{+0.20}_{-0.19}$	$18.30^{+0.20}_{-0.19}$	$18.39^{+0.19}_{-0.19}$	$18.38^{+0.20}_{-0.19}$	$18.38^{+0.20}_{-0.19}$						
UrsaMajor2	$19.54^{+0.38}_{-0.38}$	$19.01^{+0.29}_{-0.28}$	$19.10^{+0.25}_{-0.24}$	$18.56^{+0.23}_{-0.24}$	$18.63^{+0.24}_{-0.24}$	$19.05^{+0.25}_{-0.25}$	$18.91^{+0.26}_{-0.26}$	$18.98^{+0.25}_{-0.25}$	$19.04^{+0.25}_{-0.24}$	$19.12^{+0.26}_{-0.27}$	$19.13^{+0.27}_{-0.27}$						
Willman1	$19.50^{+0.44}_{-0.44}$	$18.85^{+0.34}_{-0.34}$	$18.95^{+0.29}_{-0.38}$	$18.04^{+0.27}_{-0.28}$	$18.14^{+0.27}_{-0.28}$	$18.59^{+0.30}_{-0.32}$	$18.86^{+0.29}_{-0.32}$	$18.70^{+0.29}_{-0.32}$	$18.84^{+0.26}_{-0.26}$	$18.86^{+0.32}_{-0.33}$	$18.92^{+0.31}_{-0.33}$						

Table 5: Same as Table 4, but for classical dSphs.

	w/o SHMR		PB13		BM13		PB19		BM18	
	flat	sat.								
Carina	17.86 ^{+0.09} _{-0.07}	17.86 ^{+0.07} _{-0.06}	17.85 ^{+0.06} _{-0.06}	17.85 ^{+0.06} _{-0.06}	17.86 ^{+0.07} _{-0.06}	17.86 ^{+0.07} _{-0.06}	17.87 ^{+0.06} _{-0.06}	17.87 ^{+0.06} _{-0.06}	17.87 ^{+0.06} _{-0.06}	17.87 ^{+0.06} _{-0.06}
Draco	18.92 ^{+0.06} _{-0.06}	18.89 ^{+0.06} _{-0.06}	18.85 ^{+0.06} _{-0.06}	18.85 ^{+0.06} _{-0.06}	18.85 ^{+0.06} _{-0.06}	18.85 ^{+0.06} _{-0.06}	18.88 ^{+0.06} _{-0.06}	18.88 ^{+0.06} _{-0.06}	18.88 ^{+0.06} _{-0.06}	18.88 ^{+0.06} _{-0.06}
Fornax	17.93 ^{+0.20} _{-0.08}	18.03 ^{+0.11} _{-0.10}	18.02 ^{+0.10} _{-0.08}	18.00 ^{+0.09} _{-0.07}	18.02 ^{+0.09} _{-0.08}	18.02 ^{+0.09} _{-0.08}	17.96 ^{+0.07} _{-0.06}	17.96 ^{+0.07} _{-0.06}	17.96 ^{+0.07} _{-0.06}	17.96 ^{+0.07} _{-0.06}
Leo1	17.80 ^{+0.22} _{-0.14}	17.71 ^{+0.10} _{-0.09}	17.73 ^{+0.08} _{-0.08}	17.73 ^{+0.11} _{-0.09}	17.74 ^{+0.12} _{-0.09}	17.74 ^{+0.12} _{-0.09}	17.78 ^{+0.14} _{-0.11}	17.78 ^{+0.14} _{-0.11}	17.78 ^{+0.14} _{-0.11}	17.78 ^{+0.14} _{-0.11}
Leo2	17.82 ^{+0.25} _{-0.20}	17.70 ^{+0.16} _{-0.14}	17.64 ^{+0.13} _{-0.11}	17.69 ^{+0.15} _{-0.13}	17.71 ^{+0.15} _{-0.14}	17.71 ^{+0.15} _{-0.14}	17.73 ^{+0.17} _{-0.14}	17.73 ^{+0.17} _{-0.14}	17.73 ^{+0.17} _{-0.14}	17.73 ^{+0.17} _{-0.14}
Sculptor	18.56 ^{+0.07} _{-0.05}	18.55 ^{+0.04} _{-0.04}	18.55 ^{+0.04} _{-0.04}	18.55 ^{+0.04} _{-0.04}	18.55 ^{+0.05} _{-0.04}	18.55 ^{+0.05} _{-0.04}	18.56 ^{+0.04} _{-0.04}	18.56 ^{+0.04} _{-0.04}	18.56 ^{+0.04} _{-0.04}	18.56 ^{+0.04} _{-0.04}
Sextans1	18.09 ^{+0.40} _{-0.16}	18.12 ^{+0.15} _{-0.13}	18.09 ^{+0.14} _{-0.11}	18.09 ^{+0.14} _{-0.12}	18.12 ^{+0.15} _{-0.12}	18.12 ^{+0.15} _{-0.12}	18.19 ^{+0.15} _{-0.13}	18.19 ^{+0.15} _{-0.13}	18.19 ^{+0.15} _{-0.13}	18.19 ^{+0.15} _{-0.13}
UrsaMinor	18.47 ^{+0.13} _{-0.09}	18.46 ^{+0.09} _{-0.08}	18.50 ^{+0.09} _{-0.08}	18.46 ^{+0.09} _{-0.08}	18.46 ^{+0.08} _{-0.07}	18.46 ^{+0.08} _{-0.07}	18.47 ^{+0.09} _{-0.08}	18.47 ^{+0.09} _{-0.08}	18.47 ^{+0.09} _{-0.08}	18.47 ^{+0.09} _{-0.08}

Table 6: The natural logarithm of Bayes factors of each model calculated according to Eq. (22). Column 1 shows the Bayes factor of sat_{18} to a reference model $\text{sat}_{10.5}$ for each dSph. Columns 2-5 shows the Bayes factors of the satellite prior and SHMR analyses to the satellite prior only analysis $\text{sat}_{10.5}$ as a reference, so as Columns 6-9 not for $\text{sat}_{10.5}$ but sat_{18} cases. By definition, positive (negative) values mean that the corresponding model is more (less) credible than the reference model.

sat. ₁₈ /sat. _{10.5} w/o SHMR	(sat. _{10.5} + SHMR)/sat. _{10.5}				(sat. ₁₈ + SHMR)/sat. ₁₈				
	PB13	BM13	PB19	BM18	PB13	BM13	PB19	BM18	
Aquarius2	0.77	-1.16	0.17	0.34	1.13	-2.16	-0.35	0.05	0.29
Bootes1	-0.01	0.34	0.20	0.17	0.09	0.12	0.10	0.21	0.11
Bootes2	-0.09	0.05	0.06	-0.05	-0.16	0.07	0.04	0.01	-0.01
CanesVenatici1	0.49	0.36	0.49	0.07	0.34	0.33	-0.01	-0.31	-0.03
CanesVenatici2	1.29	-0.70	0.64	0.92	2.08	-2.61	-0.70	0.15	0.71
Carina2	-0.14	0.65	0.44	0.03	-0.35	0.76	0.30	0.29	-0.19
ComaBerenices	1.06	-1.71	-0.09	0.35	1.75	-3.07	-0.52	0.07	0.64
Draco2	0.16	0.10	0.10	0.04	0.24	-0.07	-0.09	-0.05	-0.01
Eridanus2	0.79	-0.22	0.76	0.94	1.53	-0.62	-0.03	0.05	0.78
Grus1	-0.30	0.34	0.14	-0.07	-0.40	0.27	0.19	0.10	-0.07
Hercules	0.88	0.58	0.96	0.59	1.06	-0.04	-0.06	-0.07	0.15
Horologium1	1.12	-3.87	-0.78	-0.44	1.25	-4.13	-0.58	-0.03	0.25
Hydrus1	-0.17	0.30	0.23	-0.20	-0.89	0.38	0.09	-0.03	-0.85
Leo4	-0.16	0.34	0.02	-0.05	-0.93	0.44	0.15	0.01	-0.72
Leo5	-0.03	0.34	0.51	0.04	0.24	-0.47	-0.15	0.31	0.45
LeoT	1.39	0.65	1.85	1.43	0.84	-0.01	0.47	0.08	-0.61
Pegasus3	1.28	-0.19	0.37	0.11	1.62	-1.65	-0.98	-0.06	0.25
Pisces2	0.27	0.49	0.26	-0.04	-0.07	0.29	-0.01	-0.11	-0.28
Reticulum2	0.96	-1.08	0.03	0.17	1.13	-1.85	-0.82	-0.12	0.13
Segue1	1.89	-2.63	-1.00	-0.27	1.36	-4.29	-1.01	-0.05	-0.41
Segue2	0.08	0.11	0.12	0.21	0.26	-0.17	-0.20	0.04	-0.10
Triangulum2	-0.65	-0.01	0.14	-0.02	-0.52	0.57	0.37	0.08	0.16
Tucana2	-0.13	-0.23	0.16	0.11	-0.09	-0.54	0.12	0.16	-0.06
Tucana3	-2.75	0.56	0.18	-0.01	-2.82	3.39	2.68	-0.08	0.08
UrsaMajor1	1.06	-5.26	-0.16	0.61	1.84	-5.30	-0.45	-0.08	0.80
UrsaMajor2	1.25	-4.98	-1.11	0.05	1.67	-5.93	-0.63	-0.21	0.37
Willman1	2.07	-3.05	-1.05	-0.62	1.71	-4.90	-1.26	-0.37	-0.29

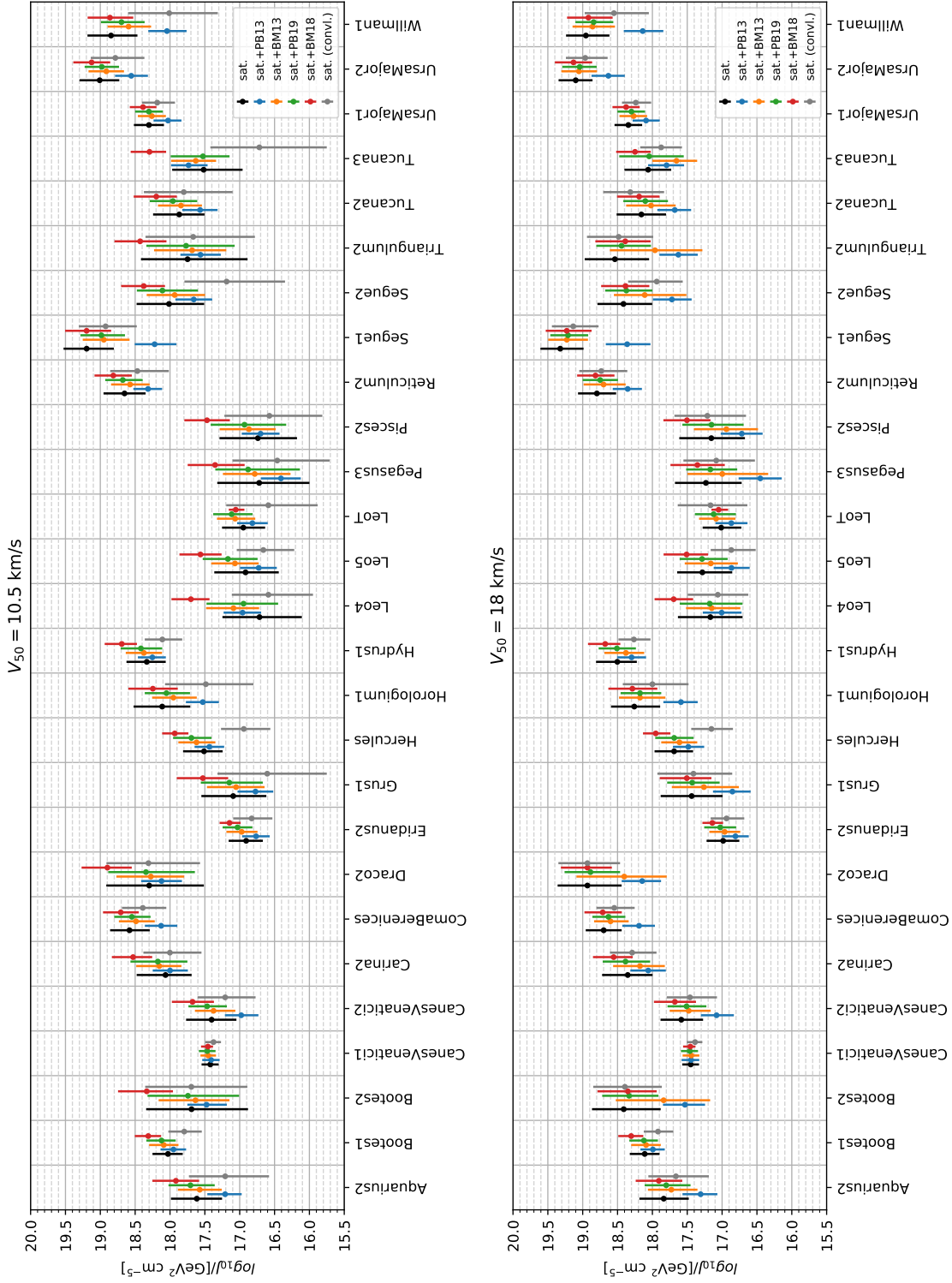


Figure 5: Estimated J -factors of UFDs in Table 4 (dots) and their 68% credible intervals (error bars). Black bars are the results with satellite prior only analysis, while gray ones show the results of conventional analysis [11]. Blue, orange, green and red bars correspond to analyses with the satellite prior and PB13, BM13, PB19 and BM18 priors, respectively. The upper panel shows results when $V_{50} = 10.5 \text{ km/s}$, while the lower panel is for $V_{50} = 18 \text{ km/s}$.

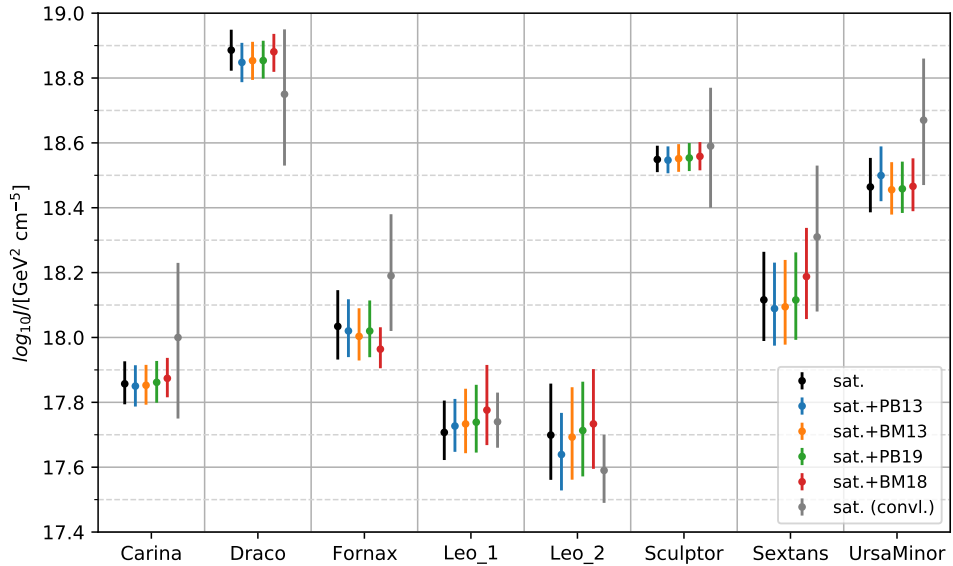


Figure 6: Same figure as Fig. 5 but for the classical dSphs listed in Table 5.

Tables 4 and 5 show the median values of J -factor posteriors with $68\% (\sim 1\sigma)$ credible intervals. Left three columns show results without SHMR priors. In particular, “flat” column denotes those without any cosmological priors (only with the likelihood and the photometry prior). Following columns are those with SHMR priors, PB13, BM13, PB19, and BM18, respectively. These results are also shown in Fig. 5. In Fig. 5, we also show the results of conventional analysis [11] as gray bars for comparison.

We show the Bayes factor of each model in Table 6. Column 1 shows the Bayes factor of sat_{18} to a reference model $\text{sat}_{10.5}$ for each dSphs. Columns 2-5 shows the Bayes factors of the satellite prior $\text{sat}_{10.5}$ and SHMR analyses to the satellite prior only analysis as a reference. Columns 6-9 are same as Columns 2-5 but for sat_{18} cases. Here a positive (negative) value indicates that the corresponding model is more (less) credible than $\text{sat}_{10.5}$.

4 Discussion

4.1 Posterior

For Boötes 2, Draco 2, Leo 4, Pegesus 3, Pisces 2, Segue 2, Triangulum 2 and Tucana 3, their posterior distributions of r_s - ρ_s without satellite priors (likelihood) are broadly distributed (Figs. 7 and 8). This is because observational errors of spectroscopic data set are too large to exclude small r_s - ρ_s region (dSph without dark matter). In such a case, the GS15-like cut excludes heavier halo mass region but estimated J -factor is still distributed broadly towards the small r_s - ρ_s region, thus the choice of scanning range of r_s and ρ_s strongly affects the result of estimation. This problem is solved by introducing the satellite prior because it excludes the small r_s - ρ_s region based on the formation history of dSphs.

For the other ultra faint dSphs, posterior distribution becomes more ridgy thanks to a large amount of kinematical data. In contrast with those obtained in SA20, the likelihood edges becomes narrow towards the upper left (compact) or lower right (faint) regions, which indicates that the height of likelihood peak varies from the upper left to the lower

right. This is thanks to the radial dependence of the velocity dispersion $\sigma(R)$; even though $\overline{\sigma}$ can be constant by varying r_s and ρ_s properly, $\sigma(R)$ cannot be kept to fit observed stellar velocity distribution at all radii.

Figure 4 shows that introducing R -dependence in the likelihood function mitigate the degeneracy between ρ_s and r_s in SA20. Since certain combinations of ρ_s and r_s gives same value of mean σ_{los}^2 , R -independent likelihood as used in SA20 has a degeneracy problem. In contrast, the function σ_{los}^2 is not equivalent even for such a combination, hence it allows us to distinguish these parameter sets. Introducing R -dependence however causes another issue, namely, arbitrariness of anisotropy function $\beta(r)$, which is just assumed to be constant for simplicity in this study. In order to remove unexpected bias, this arbitrariness should be carefully treated in the further study as well as other arbitrariness such as the axisymmetrisity.

4.2 J -factor and Bayes factor

Figure 5 shows that, in the satellite prior only analysis, our estimates of log- J -factor are larger by $\sim \mathcal{O}(0.1)$ than those estimated in SA20. This is because the R -dependence of our likelihood function weakens the ρ_s - r_s degeneracy, as mentioned in the previous section, and excludes too compact (small r_s , large ρ_s) or faint (large r_s , small ρ_s) dark matter halo with small J -factor value.

Figure 5 also shows that SHMR priors decrease the uncertainty of J -factor by up to about 50%, but estimated median values have SHMR model dependence and some estimations are not consistent with each other. For instance, the PB13 prior tends to predict smaller J -factor than other priors for dSphs with large J -factors such as Segue 1. Conversely, the BM18 prior gives larger J -factor than other priors for small J -factor dSphs such as Leo 4. These features come from the difference of SHMR models. As shown in Fig. 2, SHMR models have different slopes for small M_h region around the mass scale of dSph halos. In particular, PB13 model has large m_*/M_h ratio, while BM18 one smaller m_*/M_h than others. Once m_* is fixed by observations, large m_*/M_h gives small M_h , and vice versa. We note that Ref. [67] reported $M/L \sim 1.6$, thus our estimates of stellar mass obtained by assuming $M/L = 1$ are potentially smaller than actual values. However, this discrepancy has no significant effect on our estimation because of the scatter of SHMR models.

Bayes factors help us understand the model dependence of the estimated J -factors. Tables 4 and 6 show that models whose estimate is deviated from the result of satellite prior only analysis tend to have small Bayes factors. For instance, the PB13 model shows $\ln \text{BF} \lesssim -3$ for Segue 1 and Willman 1, and the BM18 shows $\ln \text{BF} \lesssim -1$ for Leo 4. It means that, in terms of the Bayesian analysis, the results of PB13 for Segue 1 and Willman 1 are very strongly less reliable than those of the satellite prior only analysis, and the results of BM18 for Leo 4 are substantially less reliable, respectively. We can understand this feature through posteriors in Figs. 7 and 8. For these dSphs, posteriors obtained by PB13 or BM18 are significantly deviated from the contour of the satellite prior only analysis, which means that these SHMR models and the satellite prior are incompatible. In contrast, models having comparable J -factors to the satellite prior only analysis have Bayes factors almost equal to or larger than the satellite prior only analysis. This tendency of the Bayes factors indicates that the estimated J -factor values with the satellite prior only analysis are stable even when considering SHMRs.

We can utilize this tendency in the opposite direction; not evaluating dark matter profiles

by using SHMRs, but evaluating SHMRs by using dark matter profiles. The relation between J -factors and Bayes factors suggest some possibilities that there are some unknown biases in the observation of these dSphs or that some SHMR models having small Bayes factors are invalid for certain ultra faint dSphs. The latter possibility could originate from the difference of the construction of these models; the [PB13](#) model predicts larger m_*/M_h values than the others around small halo mass region, while those of the [BM18](#) model is smaller than the others (see Fig. 2). In particular, Ref. [36] indicated that [PB13](#) assumed a strong surface-brightness incompleteness correction for faint galaxies that is no longer observationally supported [68], which causes the overestimate of the SHMR around low halo mass region. For [BM18](#), Ref. [37] pointed out that the underestimate of the [BM18](#) model around low-halo mass region occurs to compensate the overestimation of the number of massive galaxies caused by the Eddington bias. Further investigation of these features would help us to improve and calibrate these SHMR models using dSph observation or reveal some unknown nature of dSphs.

Since the J -factor values of the ultra faint dSphs obtained in this work are not significantly different from conventional values, there are no significant updates for the current dark matter constraints of the indirect detection experiment. The detection sensitivity depends on the lower bounds of J -factors. Because J -factors of dSphs with the largest J -factors such as Segue 1 and Ursa Major 2 do not change significantly even when considering cosmological priors having largest Bayes factors, constraints on dark matter parameters do also not show significant difference. The constraints however could be updated when only we select a part of dSphs as detection targets, where J -factor lower bound of each dSph matters.

In contrast, from Table 5 and Fig. 6, the J -factor uncertainty of classical dSphs obtained in this work are reduced up to about 20% of the results of [SA20](#) due to the consideration of R -dependence of the velocity dispersion. In particular, the Draco dSph, having one of the largest J -factors, has larger lower bound by about 0.25 in logarithmic scale than [SA20](#). Since indirect detection sensitivity reflects the lower bound of J -factor, the sensitivity might be stronger than the results of [SA20](#). Here we should note that our results has implicit bias of dSph model construction. In other conventional works such as Ref. [8] the uncertainty of dark matter profile is taken into account by introducing more general dark matter profile models and they indicate the deviation of dark matter profile from the simple NFW profile. In this paper, however, we neglect the uncertainty of dark matter profile by fixing it to be the NFW profile and also the that of the anisotropy profile by assuming constant model, thus our results have an implicit bias based on the model construction. In order to calculate more reliable J -factor values, we need further investigation to implement the flexibility of dark matter profile into the cosmological prior analysis.

5 Summary and conclusion

In this paper, we utilized two cosmological priors (satellite and SHMR) and a likelihood function with radial dependence to obtain better constraints on the dark matter halo profile of dSphs through the kinematical fitting using spherical Jeans equation. We prepared some different setups for the cosmological priors and estimate the posterior probability density function and J -factor. We compared these models and showed that our J -factor estimates obtained by using the satellite prior are stable in terms of their Bayes factors even when considering another cosmological prior, the SHMR prior. Cosmological priors and the R-dependence of the likelihood mitigates the degeneracy between parameters and decrease

the uncertainty of J -factor values upto about 50% for ultrafaint dSphs and about 20% for classical dSphs. These estimates would be updated by introducing the flexibility of dSph models (e.g. anisotropy, halo profile and non-sphericity).

Acknowledgements

This research made use of Astropy,⁷ a community-developed core Python package for Astronomy [69, 70], NumPy,⁸ the fundamental package for scientific computing with Python [71], and pandas,⁹ a fast, powerful, flexible and easy to use open source data analysis and manipulation tool, built on top of the Python programming language [72, 73]. This work was supported by NEXT KAKENHI Grant Numbers, JP20H05850 (S.H. and S.A.), JP20H05861 (S.A.), JSPS KAKENHI Grant Numbers, JP20H01895, JP21K13909 and JP21H05447 (K.H.). Kavli IPMU is supported by World Premier International Research Centre Initiative (WPI), MEXT, Japan.

A Posteriors

Posterior probability density distribution projected onto r_s - ρ_s plane are shown in Figs. 7 to 9. Here Figs. 7 and 8 are for ultra faint dSphs, while Fig. 9 is for classical dSphs.

⁷<http://www.astropy.org>

⁸<https://numpy.org/>

⁹<https://pandas.pydata.org/>

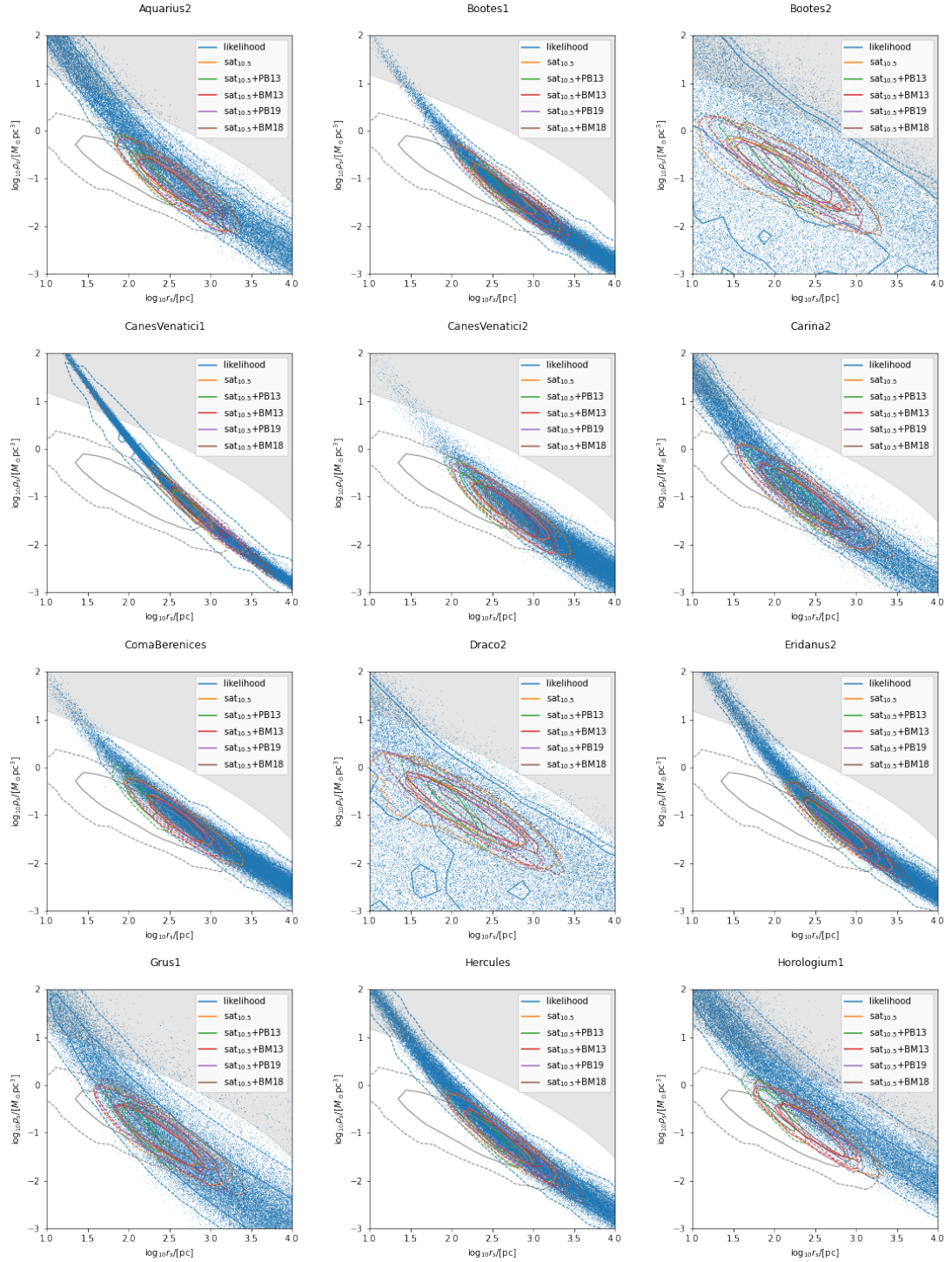


Figure 7: Posterior probability density distribution projected onto r_s - ρ_s plain with $\text{sat.}10.5$ prior. The gray shaded area shows the cosmological constraint adopted in Ref. [8]. The gray contours shows the probability density distribution of is the satellite prior $\text{sat.}10.5$. The blue dots and contours illustrate the shape of the likelihood function (flat prior). Colored contours shows the posterior probability density distribution assuming our cosmological priors.

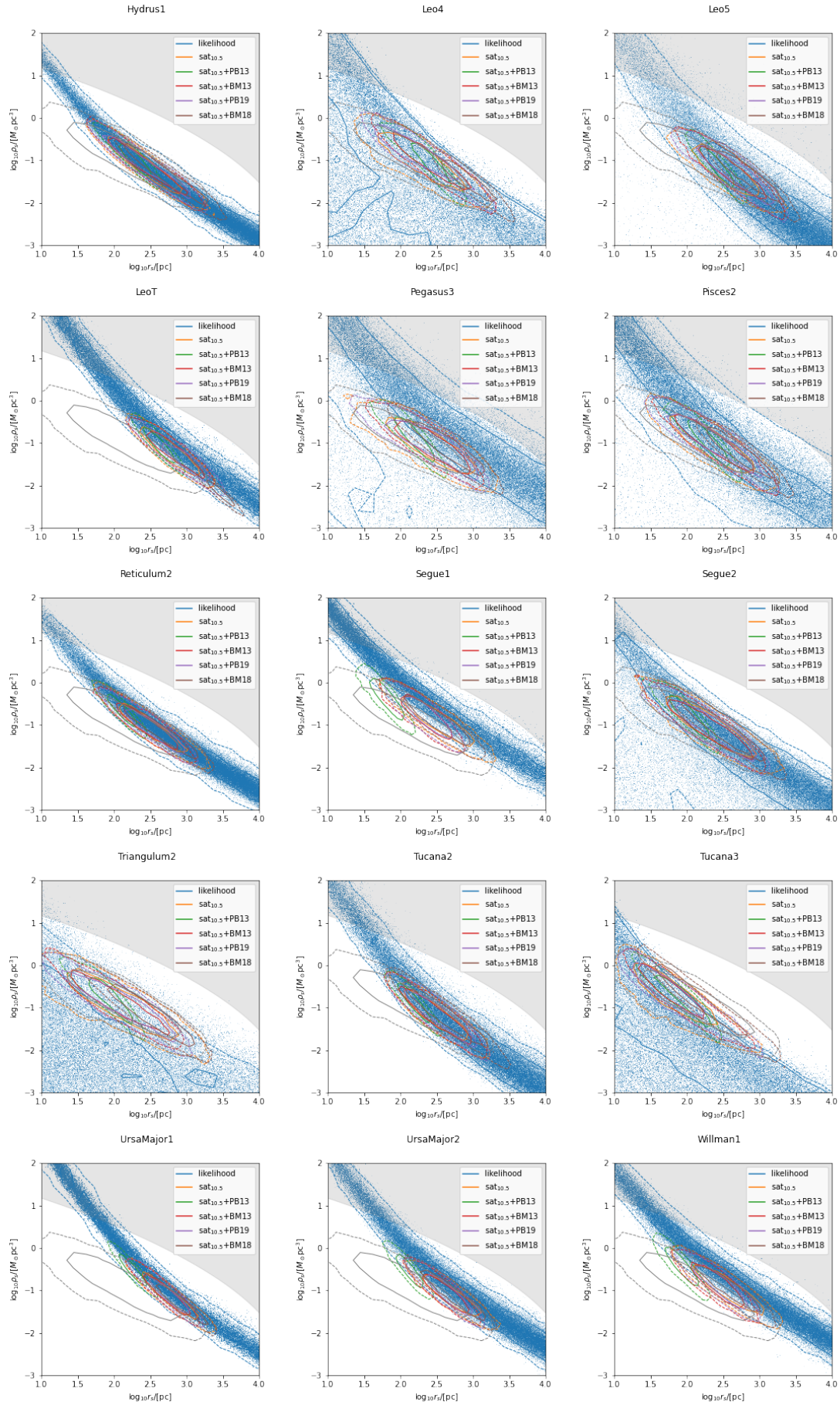


Figure 7 (cont.):

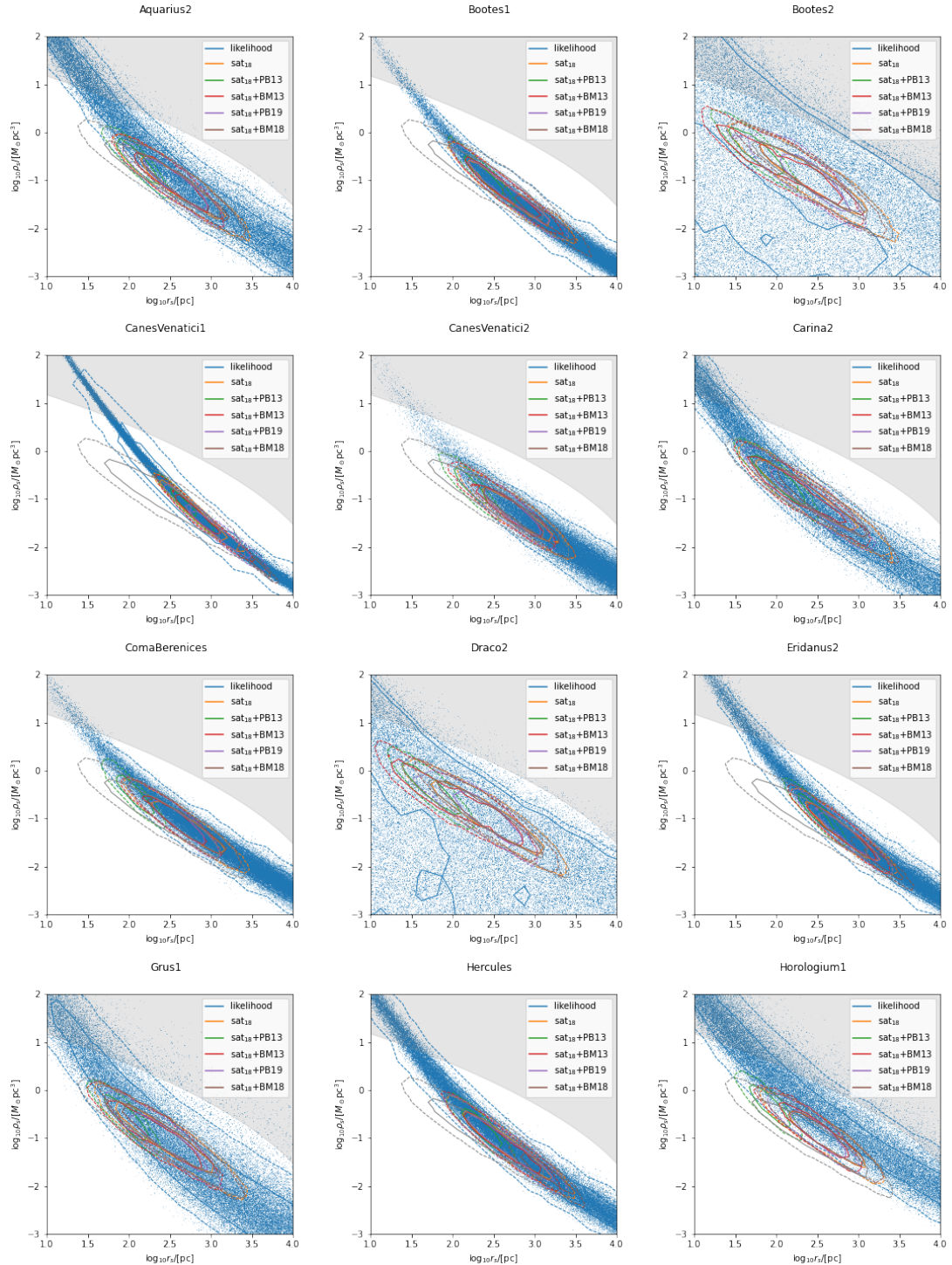


Figure 8: Same figure as Fig. 7 but using the satellite prior sat._{18} .

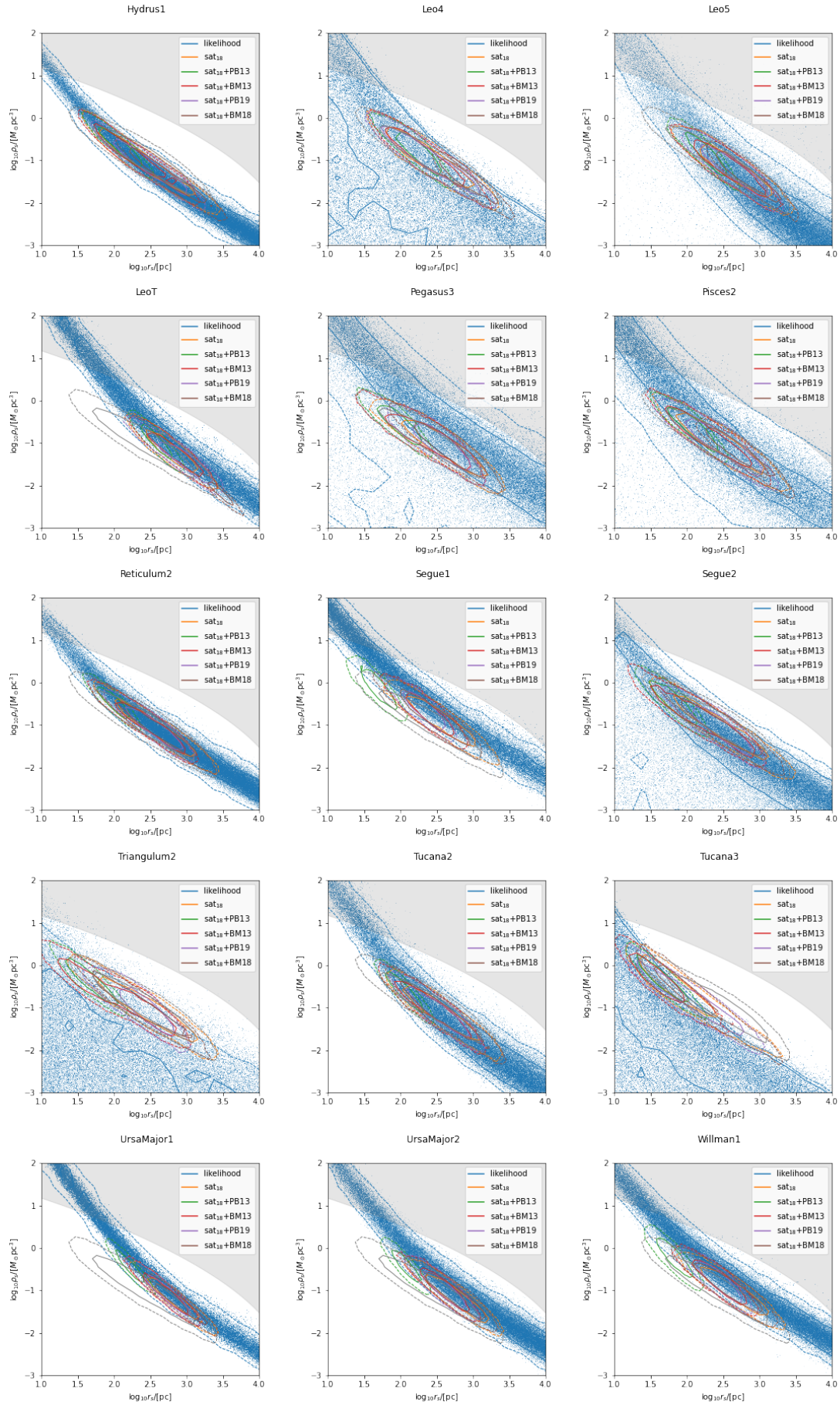


Figure 8 (cont.):

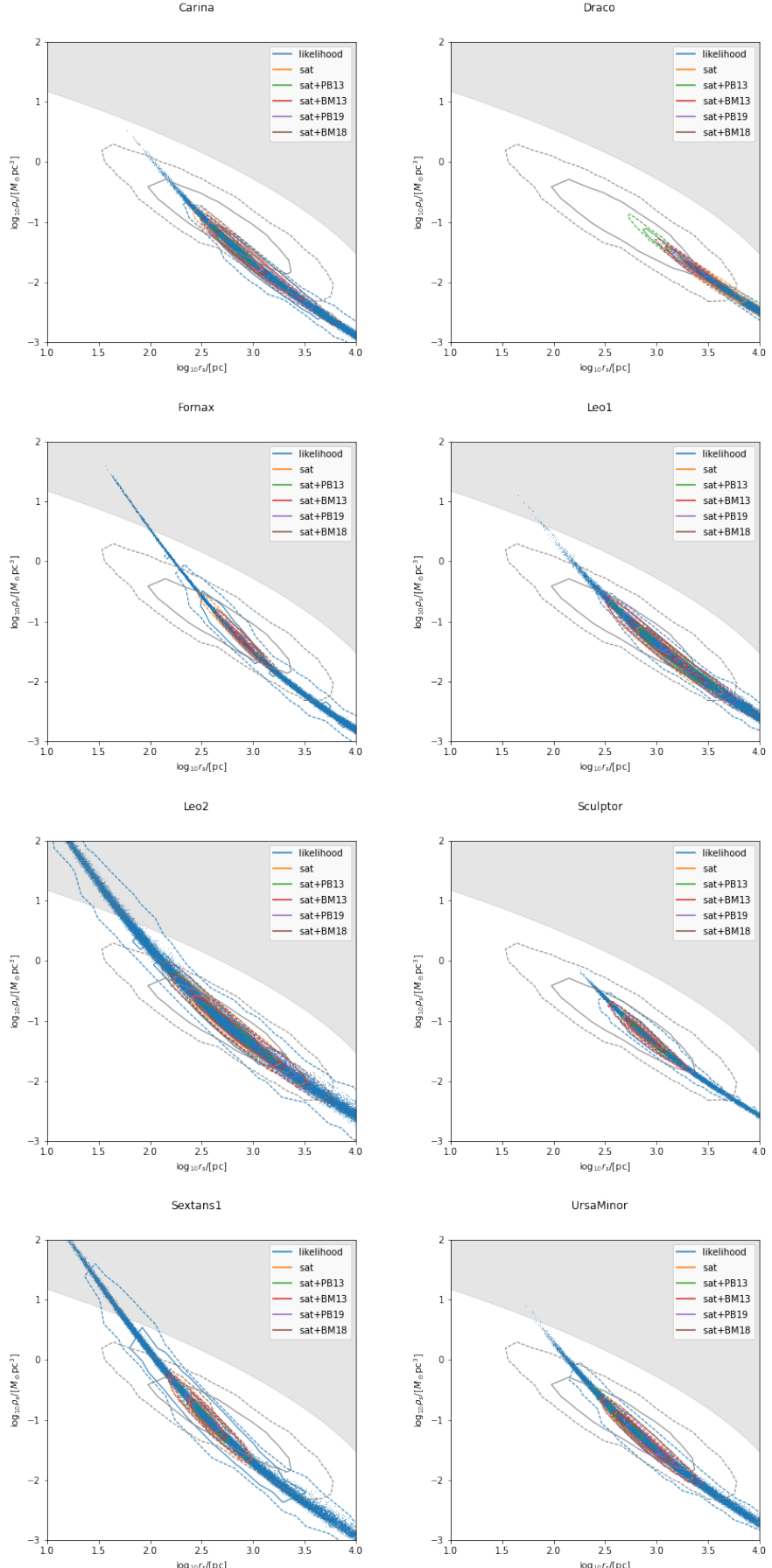


Figure 9: Same figure as Figs. 7 and 8 but for classical dSphs.

References

- [1] N. Aghanim et al. Planck 2018 results. VI. Cosmological parameters. *Astron. Astrophys.*, 641:A6, 2020. [Erratum: *Astron. Astrophys.* 652, C4 (2021)].
- [2] Jonathan L. Feng. Dark Matter Candidates from Particle Physics and Methods of Detection. *Ann. Rev. Astron. Astrophys.*, 48:495–545, 2010.
- [3] Biplob Bhattacherjee, Masahiro Ibe, Koji Ichikawa, Shigeki Matsumoto, and Kohei Nishiyama. Wino Dark Matter and Future dSph Observations. *JHEP*, 07:080, 2014.
- [4] Shin’ichiro Ando and Koji Ishiwata. Sommerfeld-enhanced dark matter searches with dwarf spheroidal galaxies. *Phys. Rev. D*, 104(2):023016, 2021.
- [5] Junji Hisano, Shigeki Matsumoto, and Mihoko M. Nojiri. Explosive dark matter annihilation. *Phys. Rev. Lett.*, 92:031303, 2004.
- [6] Junji Hisano, Shigeki Matsumoto, Mihoko M. Nojiri, and Osamu Saito. Non-perturbative effect on dark matter annihilation and gamma ray signature from galactic center. *Phys. Rev. D*, 71:063528, 2005.
- [7] James Binney and Scott Tremaine. *Galactic dynamics*. 1987.
- [8] Alex Geringer-Sameth, Savvas M. Koushiappas, and Matthew Walker. Dwarf galaxy annihilation and decay emission profiles for dark matter experiments. *Astrophys. J.*, 801(2):74, 2015.
- [9] Nagisa Hiroshima, Shin’ichiro Ando, and Tomoaki Ishiyama. Modeling evolution of dark matter substructure and annihilation boost. *Phys. Rev. D*, 97(12):123002, 2018.
- [10] Shin’ichiro Ando, Tomoaki Ishiyama, and Nagisa Hiroshima. Halo Substructure Boosts to the Signatures of Dark Matter Annihilation. *Galaxies*, 7(3):68, 2019.
- [11] Shin’ichiro Ando, Alex Geringer-Sameth, Nagisa Hiroshima, Sebastian Hoof, Roberto Trotta, and Matthew G. Walker. Structure formation models weaken limits on WIMP dark matter from dwarf spheroidal galaxies. *Phys. Rev. D*, 102(6):061302, 2020.
- [12] Julio F. Navarro, Carlos S. Frenk, and Simon D. M. White. A Universal Density Profile from Hierarchical Clustering. *ApJ*, 490(2):493–508, December 1997.
- [13] Risa H. Wechsler and Jeremy L. Tinker. The Connection between Galaxies and their Dark Matter Halos. *Ann. Rev. Astron. Astrophys.*, 56:435–487, 2018.
- [14] Kohei Hayashi, Koji Ichikawa, Shigeki Matsumoto, Masahiro Ibe, Miho N. Ishigaki, and Hajime Sugai. Dark matter annihilation and decay from non-spherical dark halos in galactic dwarf satellites. *Mon. Not. Roy. Astron. Soc.*, 461(3):2914–2928, 2016.
- [15] V. Bonnivard et al. Dark matter annihilation and decay in dwarf spheroidal galaxies: The classical and ultrafaint dSphs. *Mon. Not. Roy. Astron. Soc.*, 453(1):849–867, 2015.
- [16] H. C. Plummer. On the problem of distribution in globular star clusters. *MNRAS*, 71:460–470, March 1911.

- [17] Kohei Hayashi, Michele Fabrizio, Ewa L. Łokas, Giuseppe Bono, Matteo Monelli, Massimo Dall’Ora, and Peter B. Stetson. Dark halo structure in the Carina dwarf spheroidal galaxy: joint analysis of multiple stellar components. *Mon. Not. Roy. Astron. Soc.*, 481(1):250–261, 2018.
- [18] Andrew B. Pace, Manoj Kaplinghat, Evan Kirby, Joshua D. Simon, Erik Tollerud, Ricardo R. Muñoz, Patrick Côté, S. G. Djorgovski, and Marla Geha. Multiple chemodynamic stellar populations of the Ursa Minor dwarf spheroidal galaxy. *Mon. Not. Roy. Astron. Soc.*, 495(3):3022–3040, 2020.
- [19] W. J. G. de Blok. The Core-Cusp Problem. *Advances in Astronomy*, 2010:789293, January 2010.
- [20] G. A. Mamon and E. L. Łokas. Dark matter in elliptical galaxies - II. Estimating the mass within the virial radius. *MNRAS*, 363:705–722, November 2005.
- [21] Xiaohu Yang, H. J. Mo, Youcai Zhang, and Frank C. van den Bosch. An Analytical Model for the Accretion of Dark Matter Subhalos. *ApJ*, 741(1):13, November 2011.
- [22] Camila A. Correa, J. Stuart B. Wyithe, Joop Schaye, and Alan R. Duffy. The accretion history of dark matter haloes - III. A physical model for the concentration-mass relation. *MNRAS*, 452(2):1217–1232, September 2015.
- [23] Tomoaki Ishiyama, Steven Rieder, Junichiro Makino, Simon Portegies Zwart, Derek Groen, Keigo Nitadori, Cees de Laat, Stephen McMillan, Kei Hiraki, and Stefan Harfst. The Cosmogrid Simulation: Statistical Properties of Small Dark Matter Halos. *ApJ*, 767(2):146, April 2013.
- [24] Fangzhou Jiang and Frank C. van den Bosch. Statistics of dark matter substructure - I. Model and universal fitting functions. *MNRAS*, 458(3):2848–2869, May 2016.
- [25] G. Efstathiou. Suppressing the formation of dwarf galaxies via photoionization. *MNRAS*, 256(2):43P–47P, May 1992.
- [26] Andrew S. Graus, James S. Bullock, Tyler Kelley, Michael Boylan-Kolchin, Shea Garrison-Kimmel, and Yuewen Qi. How low does it go? Too few Galactic satellites with standard reionization quenching. *MNRAS*, 488(4):4585–4595, October 2019.
- [27] Anne A. Thoul and David H. Weinberg. Hydrodynamic Simulations of Galaxy Formation. II. Photoionization and the Formation of Low-Mass Galaxies. *ApJ*, 465:608, July 1996.
- [28] Nickolay Y. Gnedin. Effect of Reionization on Structure Formation in the Universe. *ApJ*, 542(2):535–541, October 2000.
- [29] Matthias Hoeft, Gustavo Yepes, Stefan Gottlöber, and Volker Springel. Dwarf galaxies in voids: suppressing star formation with photoheating. *MNRAS*, 371(1):401–414, September 2006.
- [30] Takashi Okamoto, Liang Gao, and Tom Theuns. Mass loss of galaxies due to an ultraviolet background. *MNRAS*, 390(3):920–928, November 2008.

- [31] Jonathan R. Hargis, Beth Willman, and Annika H. G. Peter. Too Many, Too Few, or Just Right? The Predicted Number and Distribution of Milky Way Dwarf Galaxies. *ApJ*, 795(1):L13, November 2014.
- [32] Pauli Virtanen, Ralf Gommers, Travis E. Oliphant, Matt Haberland, Tyler Reddy, David Cournapeau, Evgeni Burovski, Pearu Peterson, Warren Weckesser, Jonathan Bright, Stéfan J. van der Walt, Matthew Brett, Joshua Wilson, K. Jarrod Millman, Nikolay Mayorov, Andrew R. J. Nelson, Eric Jones, Robert Kern, Eric Larson, C J Carey, İlhan Polat, Yu Feng, Eric W. Moore, Jake VanderPlas, Denis Laxalde, Josef Perktold, Robert Cimrman, Ian Henriksen, E. A. Quintero, Charles R. Harris, Anne M. Archibald, Antônio H. Ribeiro, Fabian Pedregosa, Paul van Mulbregt, and SciPy 1.0 Contributors. SciPy 1.0: Fundamental Algorithms for Scientific Computing in Python. *Nature Methods*, 17:261–272, 2020.
- [33] Risa H. Wechsler and Jeremy L. Tinker. The Connection Between Galaxies and Their Dark Matter Halos. *ARA&A*, 56:435–487, September 2018.
- [34] Peter S. Behroozi, Risa H. Wechsler, and Charlie Conroy. The Average Star Formation Histories of Galaxies in Dark Matter Halos from $z = 0\text{--}8$. *ApJ*, 770(1):57, June 2013.
- [35] Benjamin P. Moster, Thorsten Naab, and Simon D. M. White. Galactic star formation and accretion histories from matching galaxies to dark matter haloes. *MNRAS*, 428(4):3121–3138, February 2013.
- [36] Peter Behroozi, Risa H. Wechsler, Andrew P. Hearin, and Charlie Conroy. UNIVERSEMACHINE: The correlation between galaxy growth and dark matter halo assembly from $z = 0\text{--}10$. *MNRAS*, 488(3):3143–3194, September 2019.
- [37] Benjamin P. Moster, Thorsten Naab, and Simon D. M. White. EMERGE - an empirical model for the formation of galaxies since $z \sim 10$. *MNRAS*, 477(2):1822–1852, June 2018.
- [38] Sumio Watanabe. A Widely Applicable Bayesian Information Criterion. *Journal of Machine Learning Research*, 14:867–897, 8 2012.
- [39] Harold Jeffreys. *The Theory of Probability*. Oxford Classic Texts in the Physical Sciences. 1939.
- [40] Alan W. McConnachie. The Observed Properties of Dwarf Galaxies in and around the Local Group. *AJ*, 144(1):4, July 2012.
- [41] G. Torrealba, S. E. Koposov, V. Belokurov, M. Irwin, M. Collins, M. Spencer, R. Ibata, M. Mateo, A. Bonaca, and P. Jethwa. At the survey limits: discovery of the Aquarius 2 dwarf galaxy in the VST ATLAS and the SDSS data. *MNRAS*, 463(1):712–722, November 2016.
- [42] Sergey E. Koposov, G. Gilmore, M. G. Walker, V. Belokurov, N. Wyn Evans, M. Fellhauer, W. Gieren, D. Geisler, L. Monaco, J. E. Norris, S. Okamoto, J. Peñarrubia, M. Wilkinson, R. F. G. Wyse, and D. B. Zucker. Accurate Stellar Kinematics at Faint Magnitudes: Application to the Boötes I Dwarf Spheroidal Galaxy. *ApJ*, 736(2):146, August 2011.
- [43] Andreas Koch, Mark I. Wilkinson, Jan T. Kleyna, Mike Irwin, Daniel B. Zucker, Vasily Belokurov, Gerard F. Gilmore, Michael Fellhauer, and N. Wyn Evans. A Spectroscopic Confirmation of the Boötes II Dwarf Spheroidal. *ApJ*, 690(1):453–462, January 2009.

- [44] Alexander P. Ji, Anna Frebel, Joshua D. Simon, and Marla Geha. High-resolution Spectroscopy of Extremely Metal-poor Stars in the Least-evolved Galaxies: Boötes II. *ApJ*, 817(1):41, January 2016.
- [45] Joshua D. Simon and Marla Geha. The Kinematics of the Ultra-faint Milky Way Satellites: Solving the Missing Satellite Problem. *ApJ*, 670(1):313–331, November 2007.
- [46] T. S. Li, J. D. Simon, A. B. Pace, G. Torrealba, K. Kuehn, A. Drlica-Wagner, K. Bechtol, A. K. Vivas, R. P. van der Marel, M. Wood, B. Yanny, V. Belokurov, P. Jethwa, D. B. Zucker, G. Lewis, R. Kron, D. L. Nidever, M. A. Sánchez-Conde, A. P. Ji, B. C. Conn, D. J. James, N. F. Martin, D. Martínez-Delgado, N. E. D. Noël, and MagLiteS Collaboration. Ships Passing in the Night: Spectroscopic Analysis of Two Ultra-faint Satellites in the Constellation Carina. *ApJ*, 857(2):145, April 2018.
- [47] Nicolas F. Martin, Marla Geha, Rodrigo A. Ibata, Michelle L. M. Collins, Benjamin P. M. Laevens, Eric F. Bell, Hans-Walter Rix, Annette M. N. Ferguson, Kenneth C. Chambers, Richard J. Wainscoat, and Christopher Waters. Is Draco II one of the faintest dwarf galaxies? First study from Keck/DEIMOS spectroscopy. *MNRAS*, 458(1):L59–L63, May 2016.
- [48] T. S. Li, J. D. Simon, A. Drlica-Wagner, K. Bechtol, M. Y. Wang, J. García-Bellido, J. Frieman, J. L. Marshall, D. J. James, L. Strigari, A. B. Pace, E. Balbinot, Y. Zhang, T. M. C. Abbott, S. Allam, A. Benoit-Lévy, G. M. Bernstein, E. Bertin, D. Brooks, D. L. Burke, A. Carnero Rosell, M. Carrasco Kind, J. Carretero, C. E. Cunha, C. B. D’Andrea, L. N. da Costa, D. L. DePoy, S. Desai, H. T. Diehl, T. F. Eifler, B. Flaugher, D. A. Goldstein, D. Gruen, R. A. Gruendl, J. Gschwend, G. Gutierrez, E. Krause, K. Kuehn, H. Lin, M. A. G. Maia, M. March, F. Menanteau, R. Miquel, A. A. Plazas, A. K. Romer, E. Sanchez, B. Santiago, M. Schubnell, I. Sevilla-Noarbe, R. C. Smith, F. Sobreira, E. Suchyta, G. Tarle, D. Thomas, D. L. Tucker, A. R. Walker, R. H. Wechsler, W. Wester, B. Yanny, and DES Collaboration. Farthest Neighbor: The Distant Milky Way Satellite Eridanus II. *ApJ*, 838(1):8, March 2017.
- [49] Matthew G. Walker, Mario Mateo, Edward W. Olszewski, Sergey Koposov, Vasily Belokurov, Prashin Jethwa, David L. Nidever, Vincent Bonnivard, III Bailey, John I., Eric F. Bell, and Sarah R. Loebman. Magellan/M2FS Spectroscopy of Tucana 2 and Grus 1. *ApJ*, 819(1):53, March 2016.
- [50] Sergey E. Koposov, Andrew R. Casey, Vasily Belokurov, James R. Lewis, Gerard Gilmore, Clare Worley, Anna Hourihane, S. Randich, T. Bensby, A. Bragaglia, M. Bergemann, G. Carraro, M. T. Costado, E. Flaccomio, P. Francois, U. Heiter, V. Hill, P. Jofre, C. Lando, A. C. Lanzafame, P. de Laverny, L. Monaco, L. Morbidelli, L. Sbordone, Š. Mikolaitis, and N. Ryde. Kinematics and Chemistry of Recently Discovered Reticulum 2 and Horologium 1 Dwarf Galaxies. *ApJ*, 811(1):62, September 2015.
- [51] Sergey E. Koposov, Matthew G. Walker, Vasily Belokurov, Andrew R. Casey, Alex Geringer-Sameth, Dougal Mackey, Gary Da Costa, Denis Erkal, Prashin Jethwa, Mario Mateo, Edward W. Olszewski, and John I. Bailey. Snake in the Clouds: a new nearby dwarf galaxy in the Magellanic bridge*. *MNRAS*, 479(4):5343–5361, October 2018.
- [52] Sydney A. Jenkins, Ting S. Li, Andrew B. Pace, Alexander P. Ji, Sergey E. Koposov, and Burçin Mutlu-Pakdil. Very Large Telescope Spectroscopy of Ultra-faint Dwarf Galaxies. I. Boötes I, Leo IV, and Leo V. *ApJ*, 920(2):92, October 2021.

- [53] Dongwon Kim, Helmut Jerjen, Marla Geha, Anirudh Chiti, Antonino P. Milone, Gary Da Costa, Dougal Mackey, Anna Frebel, and Blair Conn. Portrait of a Dark Horse: a Photometric and Spectroscopic Study of the Ultra-faint Milky Way Satellite Pegasus III. *ApJ*, 833(1):16, December 2016.
- [54] Evan N. Kirby, Joshua D. Simon, and Judith G. Cohen. Spectroscopic Confirmation of the Dwarf Galaxies Hydra II and Pisces II and the Globular Cluster Laevens 1. *ApJ*, 810(1):56, September 2015.
- [55] J. D. Simon, A. Drlica-Wagner, T. S. Li, B. Nord, M. Geha, K. Bechtol, E. Balbinot, E. Buckley-Geer, H. Lin, J. Marshall, B. Santiago, L. Strigari, M. Wang, R. H. Wechsler, B. Yanny, T. Abbott, A. H. Bauer, G. M. Bernstein, E. Bertin, D. Brooks, D. L. Burke, D. Capozzi, A. Carnero Rosell, M. Carrasco Kind, C. B. D’Andrea, L. N. da Costa, D. L. DePoy, S. Desai, H. T. Diehl, S. Dodelson, C. E. Cunha, J. Estrada, A. E. Evrard, A. Fausti Neto, E. Fernandez, D. A. Finley, B. Flaugher, J. Frieman, E. Gaztanaga, D. Gerdes, D. Gruen, R. A. Gruendl, K. Honscheid, D. James, S. Kent, K. Kuehn, N. Kuropatkin, O. Lahav, M. A. G. Maia, M. March, P. Martini, C. J. Miller, R. Miquel, R. Ogando, A. K. Romer, A. Roodman, E. S. Rykoff, M. Sako, E. Sanchez, M. Schubnell, I. Sevilla, R. C. Smith, M. Soares-Santos, F. Sobreira, E. Suchyta, M. E. C. Swanson, G. Tarle, J. Thaler, D. Tucker, V. Vikram, A. R. Walker, W. Wester, and DES Collaboration. Stellar Kinematics and Metallicities in the Ultra-faint Dwarf Galaxy Reticulum II. *ApJ*, 808(1):95, July 2015.
- [56] Joshua D. Simon, Marla Geha, Quinn E. Minor, Gregory D. Martinez, Evan N. Kirby, James S. Bullock, Manoj Kaplinghat, Louis E. Strigari, Beth Willman, Philip I. Choi, Erik J. Tollerud, and Joe Wolf. A Complete Spectroscopic Survey of the Milky Way Satellite Segue 1: The Darkest Galaxy. *ApJ*, 733(1):46, May 2011.
- [57] Evan N. Kirby, Michael Boylan-Kolchin, Judith G. Cohen, Marla Geha, James S. Bullock, and Manoj Kaplinghat. Segue 2: The Least Massive Galaxy. *ApJ*, 770(1):16, June 2013.
- [58] Evan N. Kirby, Judith G. Cohen, Joshua D. Simon, Puragra Guhathakurta, Anders O. Thygesen, and Gina E. Duggan. Triangulum II. Not Especially Dense After All. *ApJ*, 838(2):83, April 2017.
- [59] J. D. Simon, T. S. Li, A. Drlica-Wagner, K. Bechtol, J. L. Marshall, D. J. James, M. Y. Wang, L. Strigari, E. Balbinot, K. Kuehn, A. R. Walker, T. M. C. Abbott, S. Allam, J. Annis, A. Benoit-Lévy, D. Brooks, E. Buckley-Geer, D. L. Burke, A. Carnero Rosell, M. Carrasco Kind, J. Carretero, C. E. Cunha, C. B. D’Andrea, L. N. da Costa, D. L. DePoy, S. Desai, P. Doel, E. Fernandez, B. Flaugher, J. Frieman, J. García-Bellido, E. Gaztanaga, D. A. Goldstein, D. Gruen, G. Gutierrez, N. Kuropatkin, M. A. G. Maia, P. Martini, F. Menanteau, C. J. Miller, R. Miquel, E. Neilsen, B. Nord, R. Ogando, A. A. Plazas, A. K. Romer, E. S. Rykoff, E. Sanchez, B. Santiago, V. Scarpine, M. Schubnell, I. Sevilla-Noarbe, R. C. Smith, F. Sobreira, E. Suchyta, M. E. C. Swanson, G. Tarle, L. Whiteway, B. Yanny, and DES Collaboration. Nearest Neighbor: The Low-mass Milky Way Satellite Tucana III. *ApJ*, 838(1):11, March 2017.
- [60] Beth Willman, Marla Geha, Jay Strader, Louis E. Strigari, Joshua D. Simon, Evan Kirby, Nhung Ho, and Alex Warres. Willman 1—A Probable Dwarf Galaxy with an Irregular Kinematic Distribution. *AJ*, 142(4):128, October 2011.

- [61] Matthew G. Walker, Mario Mateo, and Edward W. Olszewski. Stellar Velocities in the Carina, Fornax, Sculptor, and Sextans dSph Galaxies: Data From the Magellan/MMFS Survey. *AJ*, 137(2):3100–3108, February 2009.
- [62] Matthew G. Walker, Edward W. Olszewski, and Mario Mateo. Bayesian analysis of resolved stellar spectra: application to MMT/Hectochelle observations of the Draco dwarf spheroidal. *MNRAS*, 448(3):2717–2732, April 2015.
- [63] Mario Mateo, Edward W. Olszewski, and Matthew G. Walker. The Velocity Dispersion Profile of the Remote Dwarf Spheroidal Galaxy Leo I: A Tidal Hit and Run? *ApJ*, 675(1):201–233, March 2008.
- [64] Meghan E. Spencer, Mario Mateo, Matthew G. Walker, and Edward W. Olszewski. A Multi-epoch Kinematic Study of the Remote Dwarf Spheroidal Galaxy Leo II. *ApJ*, 836(2):202, February 2017.
- [65] Meghan E. Spencer, Mario Mateo, Edward W. Olszewski, Matthew G. Walker, Alan W. McConnachie, and Evan N. Kirby. The Binary Fraction of Stars in Dwarf Galaxies: The Cases of Draco and Ursa Minor. *AJ*, 156(6):257, December 2018.
- [66] Daniel Foreman-Mackey, David W. Hogg, Dustin Lang, and Jonathan Goodman. emcee: The MCMC Hammer. *PASP*, 125(925):306, March 2013.
- [67] Joanna Woo, Stéphane Courteau, and Avishai Dekel. Scaling relations and the fundamental line of the local group dwarf galaxies. *MNRAS*, 390(4):1453–1469, November 2008.
- [68] Richard P. Williams, I. K. Baldry, L. S. Kelvin, P. A. James, S. P. Driver, M. Prescott, S. Brough, M. J. I. Brown, L. J. M. Davies, B. W. Holwerda, J. Liske, P. Norberg, A. J. Moffett, and A. H. Wright. Galaxy And Mass Assembly (GAMA): detection of low-surface-brightness galaxies from SDSS data. *MNRAS*, 463(3):2746–2755, December 2016.
- [69] Thomas P Robitaille, Erik J Tollerud, Perry Greenfield, Michael Droettboom, Erik Bray, Tom Aldcroft, Matt Davis, Adam Ginsburg, Adrian M Price-Whelan, Wolfgang E Kerzendorf, Alexander Conley, Neil Crighton, Kyle Barbary, Demitri Muna, Henry Ferguson, Frédéric Grollier, Madhura M Parikh, Prasanth H Nair, Hans M Günther, Christoph Deil, Julien Woillez, Simon Conseil, Roban Kramer, James E H Turner, Leo Singer, Ryan Fox, Benjamin A Weaver, Victor Zabalza, Zachary I Edwards, K. Azalee Bostroem, D J Burke, Andrew R Casey, Steven M Crawford, Nadia Dencheva, Justin Ely, Tim Jenness, Kathleen Labrie, Pey Lian Lim, Francesco Pierfederici, Andrew Pontzen, Andy Ptak, Brian Refsdal, Mathieu Servillat, and Ole Streicher. Astropy: A community Python package for astronomy. *A&A*, 558:A33, 10 2013.
- [70] A. M. Price-Whelan, B M Sipőcz, H M Günther, P L Lim, S M Crawford, S Conseil, D L Shupe, M W Craig, N Dencheva, A Ginsburg, J. T. VanderPlas, L D Bradley, D Pérez-Suárez, M. de Val-Borro, T L Aldcroft, K L Cruz, T P Robitaille, E J Tollerud, C Ardelean, T Babej, Y P Bach, M Bachetti, A V Bakanov, S P Bamford, G Barentsen, P Barmby, A Baumbach, K L Berry, F Biscani, M Boquien, K A Bostroem, L G Bouma, G B Brammer, E M Bray, H Breytenbach, H Buddelmeijer, D J Burke, G Calderone, J. L. Cano Rodríguez, M Cara, J V M Cardoso, S. Cheedella, Y. Copin, L. Corrales, D Crichton,

D. D'Avella, C Deil, É Depagne, J P Dietrich, A Donath, M Droettboom, N Earl, T Erben, S Fabbro, L A Ferreira, T Finethy, R T Fox, L H Garrison, S L J Gibbons, D A Goldstein, R Gommers, J P Greco, P Greenfield, A M Groener, F Grollier, A Hagen, P Hirst, D Homeier, A J Horton, G Hosseinzadeh, L Hu, J S Hunkeler, Ž Ivezić, A Jain, T Jeness, G Kanarek, S Kendrew, N S Kern, W E Kerzendorf, A Khvalko, J King, D Kirkby, A M Kulkarni, A Kumar, A Lee, D Lenz, S P Littlefair, Z Ma, D M Macleod, M Mastropietro, C. McCully, S Montagnac, B M Morris, M Mueller, S J Mumford, D Muna, N A Murphy, S Nelson, G H Nguyen, J P Ninan, M Nöthe, S Ogaz, S Oh, J K Parejko, N Parley, S Pascual, R. Patil, A A Patil, A L Plunkett, J X Prochaska, T Rastogi, V. Reddy Janga, J Sabater, P Sakurikar, M Seifert, L E Sherbert, H Sherwood-Taylor, A Y Shih, J Sick, M T Silbiger, S Singanamalla, L P Singer, P H Sladen, K A Sooley, S Sornarajah, O Streicher, P Teuben, S W Thomas, G R Tremblay, J E H Turner, V Terrón, M. H. van Kerkwijk, A. de la Vega, L L Watkins, B A Weaver, J B Whitmore, J Woillez, and V Zabalza. The Astropy Project: Building an Open-science Project and Status of the v2.0 Core Package. *AJ*, 156(3):123, 8 2018.

- [71] Charles R. Harris, K. Jarrod Millman, Stéfan J. van der Walt, Ralf Gommers, Pauli Virtanen, David Cournapeau, Eric Wieser, Julian Taylor, Sebastian Berg, Nathaniel J. Smith, Robert Kern, Matti Picus, Stephan Hoyer, Marten H. van Kerkwijk, Matthew Brett, Allan Haldane, Jaime Fernández del Río, Mark Wiebe, Pearu Peterson, Pierre Gérard-Marchant, Kevin Sheppard, Tyler Reddy, Warren Weckesser, Hameer Abbasi, Christoph Gohlke, and Travis E. Oliphant. Array programming with NumPy. *Nature*, 585(7825):357–362, September 2020.
- [72] The pandas development team. pandas-dev/pandas: Pandas 1.2.4, April 2021.
- [73] Wes McKinney. Data Structures for Statistical Computing in Python. In Stéfan van der Walt and Jarrod Millman, editors, *Proceedings of the 9th Python in Science Conference*, pages 56 – 61, 2010.